Tellus B
Chemical and Physical Meteorology

Exploring the Sensitivity of Arctic Winter Climate to Aerosol Loading as Simulated in CMIP6

ORIGINAL RESEARCH PAPER

KHALED AL HAJJAR
OLIVIA LINKE
SUDHAKER DIPU
KARSTEN HAUSTEIN
JOHANNES QUAAS

*Author affiliations can be found in the back matter of this article

STOCKHOLM UNIVERSITY PRESS

ABSTRACT

Using model output from the Radiative Forcing Model Intercomparison Project (RFMIP), endorsed by the sixth Coupled Model Intercomparison Project 6 (CMIP6), we investigated the impact of aerosols on the Arctic climate (averaged over the region north of 66°N) during winter. The average of these models shows that the present-day aerosols (as of the year 2014) result in a positive aerosol effective radiative forcing (ERF_{aer}) of approximately 0.14 $W\,m^{-2}$ in the Arctic during winter, relative to pre-industrial conditions defined as those of the year 1850. This positive ERF_{aer} is associated with enhanced aerosol loading through strong transport from Eurasia and adjoining regions, causing the Arctic region to warm by up to 1 K in the present-day compared to the pre-industrial conditions. The Arctic warming attributed to aerosols also significantly affects climate variability, particularly the Arctic Oscillation (AO). Present-day aerosols resulted in a positively skewed distribution of the Arctic Oscillation index (AOI) compared to the control simulation, reflecting a shift toward more frequent positive AO phases associated with negative sea level pressure (SLP) anomalies across the northern Atlantic, Pacific, and Eurasian regions, and positive SLP anomalies over northern North America. Additionally, the transient experiment, which includes time-varying aerosol emissions, is used to investigate the sensitivity of Arctic winter climate to the aerosol enhancement, based on low and high aerosol scenarios. During the high aerosol scenario, warming in near-surface air temperature (SAT) is concentrated over the Arctic region, reaching approximately 1 K, while less warming is simulated in the low aerosol scenario. The AOI distribution is positively skewed in both aerosol scenarios, indicating that changes in aerosol concentrations influence the AO. However, the skewness is weaker under the high aerosol scenario compared to the low aerosol case, suggesting that stronger aerosol forcing tends to stabilize the AO and limit its variability. Nevertheless, increased sensitivity of the AO to aerosol can lead to extreme weather, particularly warmer winters in the Arctic, in contrast to most of the Northern Hemisphere, regardless of the AO phase. Our analysis also suggests that aerosol enhancement contributes to a shift in the jet stream's position. Furthermore, the lapse rate feedback (LRF), a contributor to the Arctic amplification, also shows an increase due to aerosol enhancement. This indicates that both the strength and magnitude of the LRF are sensitive to aerosol concentrations, which may further intensify Arctic warming/amplification.

CORRESPONDING AUTHOR:
Khaled Al Hajjar
Institute for Meteorology, Leipzig University, Leipzig, Germany
khajjar@uni-leipzig.de

KEYWORDS:
Arctic amplification; aerosol radiative forcing; Arctic Oscillation; lapse rate feedback; CMIP6; RFMIP

TO CITE THIS ARTICLE:
Al Hajjar, K., Dipu, S., Quaas, J., Linke, O. and Haustein, K. (2025) Exploring the Sensitivity of Arctic Winter Climate to Aerosol Loading as Simulated in CMIP6. *Tellus B: Chemical and Physical Meteorology* 77(1): 20–40. DOI: https://doi.org/10.16993/tellusb.1885

1. INTRODUCTION

The global near-surface atmospheric temperature (SAT) has increased over time since the 19th century, and the most warming occurred in the recent decades after 1975 (Hansen *et al.*, 2010; Morice *et al.*, 2021; Craigmile and Guttorp, 2021). The recent warming over the land is more significant than that of the oceans, and the most affected regions are the high northern latitudes (Morice *et al.*, 2021). In the Arctic, the average temperature north of 66.5°N has increased approximately four times more than the global increase between 1979 and 2021, referred to as Arctic amplification, though this warming difference differs by season and depends on the time period considered (Rantanen *et al.*, 2022). Wendisch *et al.* (2023) also observed that the Arctic region north of 60°N has warmed faster than the lower latitudes between 20°S and 60°N, particularly in spring and winter, but this trend is less observed in summer. The enhanced Arctic warming is caused by many factors, including sea ice loss (Dai *et al.*, 2019), enhanced heat and moisture transport in the atmosphere from the North Atlantic into the Arctic (Alekseev *et al.*, 2020), and local climate feedbacks within the Arctic region (Block *et al.*, 2020). Several reasons are behind the lower Arctic warming in summer, which mainly include the large heat uptake by the Arctic Ocean in summer and its release into the atmosphere in autumn and early winter (Laîné *et al.*, 2016), as well as the larger increase in the evaporation rate over the ice-free Arctic lands in summer compared to winter (Laîné *et al.*, 2016).

The recent global climate change is mainly caused by anthropogenic emissions of greenhouse gases (GHG) like carbon dioxide (CO_2), methane (CH_4) and nitrous oxide (N_2O) (Ciais *et al.*, 2013). These gases modify the atmospheric energy balance by absorbing the upward long wave radiation and then emitting it in different directions (Kiehl and Trenberth, 1997). A part of the emission is directed downward, which reduces the heat loss from the surface and the lower atmosphere. Besides the GHGs, the anthropogenic emissions of aerosols have a significant impact on the global climate (Myhre *et al.*, 2013). Atmospheric aerosols are liquid or solid particles suspended in the air that impact the climate through scattering and absorption of incoming solar radiation, as well as through interactions with terrestrial radiation via absorption and re-emission, referred to as the direct effect (Naik *et al.*, 2021). Atmospheric aerosol also affects the climate indirectly by acting aerosol as cloud condensation nuclei (CCN, Twomey, 1974) and ice nucleating particles (INP, DeMott *et al.*, 2010) through modifying the cloud micro- and macro-physical properties that are related to the cloud-radiation interactions like the cloud albedo. The effects of aerosols on the global climate differ by the aerosol type, but their overall impact, represented by the effective radiative forcing (ERF_{aer})—which includes both direct and indirect effects of the aerosols—is estimated as a cooling effect in the context of human-induced climate change reducing a part of the GHG warming, with uncertainties about the impact's magnitude, which is estimated to be between −2.0 to −0.4 W m^{-2} with a 90% likelihood in the period 2005 to 2015 compared to 1850 (Bellouin *et al.*, 2020).

Several responses occur in the climate system due to the impacts of the anthropogenic emissions of GHG and aerosols on the climate. These responses include changes in water evaporation rates and alterations in the extent of sea ice and vegetation, which in turn affect surface albedo. Such changes can influence the atmospheric energy balance differently across various regions, seasons, and altitudes, leading to varying rates of cooling and warming (Mauritsen *et al.*, 2013). Although climate change is globally observed, several studies have focused on specific regions due to their significant impacts and responses to climate change. One of these regions is the Arctic, which is experiencing some of the most pronounced warming effects of global climate change. The melting ice in Greenland contributes to rising global sea levels (Pritchard *et al.*, 2009). Many studies on Arctic warming have revealed that various mechanisms contribute to this warming beyond the GHG forcing (Taylor *et al.*, 2022; Previdi *et al.*, 2021). For instance, Previdi *et al.* (2021) reported that aerosol forcing has been found to warm the Arctic SAT despite its cooling effect on the globe.

In addition to global climate change, there are natural fluctuations in the form of climate variability, individually known as modes of oscillations. One of these is the Arctic Oscillation (AO), which is presented as the leading mode of interannual atmospheric variability in the northern hemisphere (NH) (Thompson and Wallace, 2000). The AO plays a vital role in shaping the climate of the NH, particularly across the Arctic and mid-latitudes. Specifically, it has a profound impact on winter weather patterns (Thompson and Wallace, 2000). The phase and strength of the AO alter the position and intensity of the jet stream, thereby modulating the prevailing circulation and associated weather systems in the NH (Thompson and Wallace, 2000). In recent years, it has been evident that the AO index (AOI), which quantifies the phase and strength of the AO, has shifted toward more negative values (Maturilli and Kayser, 2017). Variability in the AO can influence the transport of heat and moisture into the Arctic from lower latitudes. This, in turn, can modify the lapse rate feedback (LRF), which refers to the change in temperature with altitude. The LRF is a crucial component of the climate system, especially in the Arctic regions, where it can amplify warming (Linke *et al.*, 2023).

As a contributor to climate change, especially by warming the Arctic, studying the influence of aerosols on the AO is sparse. Using the community atmosphere

model, Allen and Sherwood (2011) suggested that the aerosol enhancement could have influenced the AO. Qu *et al.* (2021) reported that volcanic aerosols strengthen the AO by intensifying the Arctic vortex system. Additionally, modeling studies have linked the Southeast Asian haze to the AO variability (e.g., Chung and Ramanathan, 2003). Moreover, increased aerosol loading in the Arctic can influence the lapse rate by altering the vertical distribution of heat (e.g., Calì Quaglia *et al.*, 2022; Stone *et al.*, 2008; Treffeisen *et al.*, 2007), which in turn affects the ERF_{aer} and the AO. Many studies, such as Salvi *et al.* (2022), have highlighted the sensitivity of LRF to aerosol changes, demonstrating that higher concentrations of aerosols can lead to changes in feedback mechanisms.

Despite the amplified Arctic warming observed in recent decades, the overall effect of aerosols on Arctic warming remains highly uncertain due to the distinctive geographical conditions and the various sources, types, and transport pathways of aerosols entering the Arctic. As a contributor to climate change, particularly in relation to Arctic warming, studying the influence of aerosols on the AO and the LRF provides valuable insights into how the aerosols affect the atmospheric circulation patterns in the NH and the sensitivity of the Arctic winter climate to these effects. This study, therefore, investigates the sensitivity of the Arctic winter climate to aerosol forcing using the Coupled Model Intercomparison Project 6 (CMIP6, Eyring *et al.*, 2016). CMIP6 provides a comprehensive set of coordinated climate model experiments that include state-of-the-art representations of aerosol radiative effects, historical and projected forcing, and Arctic-relevant processes, making it particularly suitable for investigating the regional climate response. We quantify how ERF_{aer} shapes the AO variability and LRF to determine the Arctic's climate response. Focusing on boreal winter allows us to isolate the radiative effects and the dynamical atmospheric responses that are most relevant to the Arctic climate change. By linking aerosol forcing to atmospheric circulation and the LRF mechanism, this work aims to improve the understanding of aerosol impact and the sensitivity of the Arctic climate to this impact.

2. DATA AND METHODS

2.1. MODELS AND EXPERIMENTAL SETUP

This work utilizes model simulations from the Radiative Forcing Model Intercomparison Project (RFMIP, Pincus *et al.*, 2016), endorsed by CMIP6 (Eyring *et al.*, 2016), to investigate the impact of aerosol radiative forcing on the AO and Arctic climate north of 66°N. The main focus of the RFMIP is to improve the understanding of radiative forcing due to anthropogenic perturbations (Smith *et al.*, 2020a). The models participating in the RFMIP are run in the atmosphere-only mode with pre-industrial climatology of fixed sea-surface temperature (SST) and sea ice distribution derived from the same model's corresponding coupled pre-industrial control run (piControl, Eyring *et al.*, 2016). This setup isolates the instantaneous atmospheric response to the forcing, enabling the study of rapid changes in the atmosphere that occur directly from the forcing itself, without the complicating effects of the ocean and sea ice changing in response.

The RFMIP provides present-day time slice experiments in which forcing agents are held constant at their present-day levels in the year 2014. This study utilizes 30-year time slice simulations with piClim-aer configuration that applies present-day aerosols (as of the year 2014) with fixed-SST settings. The 30-year reference simulation, piClim-control, maintains forcing components at pre-industrial levels (1850) and serves in our study as a baseline for estimating present-day ERF_{aer} and their impacts on Arctic climate. Table 1 summarizes the models in piClim-control and piClim-aer used in this analysis, which were obtained from the Earth System Grid Federation (ESGF, https://esgf.llnl.gov/).

The RFMIP also provides historical-to-future transient experiments, in which the forcing agents' concentrations evolve over time (Pincus *et al.*, 2016). The transient experiments are designed to understand the CMIP6 historical transient ERF and the potential future radiative forcing. To analyze the evolution of aerosols' impact on the Arctic climate, we have adopted the model simulations from piClim-histaer. The selected simulations consist of applied historical transient aerosols between 1850 and 2014 (Eyring *et al.*, 2016) and future aerosol emissions between 2015 and 2100 under the Shared Socioeconomic Pathway SSP2-4.5 scenario that represents a moderate level of radiative forcing (O'Neill *et al.*, 2016). All other conditions in these simulations are set at pre-industrial. In the transient case also, the reference piClim-control simulation is used as the baseline for the analysis. The used models of this experiment are shown in Table 2.

To investigate the impact of aerosol on the Arctic climate and its variability under the AO, the analysis is restricted to the NH between 20° to 90°N. Further, the analysis is limited to the winter season, covering the months of December, January, and February (DJF), because AO is present at its maximum during boreal winter. Data in January and February of the first year in every period were avoided due to the inability to calculate the winter average of the first year. The winter average will be presented starting from the second year in each period. For the analysis, we have used monthly mean datasets from the model simulations. In all analyses, the multi-model mean was evaluated with respect to the reference baseline simulation. For the calculation of the

MODELS	MODEL REFERENCE	DATA REFERENCE	COUNT OF RUNS (piClim-control, piClim-aer)
CNRM-CM6-1	Voldoire *et al.* (2019)	Voldoire (2019a;b)	1, 1
CNRM-ESM2-1	Séférian *et al.* (2019)	Seferian (2019a;b)	1, 1
CanESM5	Swart *et al.* (2019)	Cole *et al.* (2019a;b)	1, 1
EC-Earth3	Döscher *et al.* (2022)	EC-Earth Consortium (2020a;b)	1, 1
IPSL-CM6A-LR-INCA	Boucher *et al.* (2020c)	Boucher *et al.* (2020a;b)	1, 1
MIROC6	Tatebe *et al.* (2019)	Sekiguchi and Shiogama (2019a;b)	1, 1
MPI-ESM-1-2-HAM	Mauritsen *et al.* (2019)	Neubauer *et al.* (2019a;b)	1, 1
MRI-ESM2-0	Yukimoto *et al.* (2019)	Yukimoto *et al.* (2019a;b)	1, 1
UKESM1-0-LL	Sellar *et al.* (2019)	O'Connor (2019a;b)	1, 1

Table 1 Models used in the time-slice simulations (30 years) for this study.

MODELS	MODEL REFERENCE	DATA REFERENCE	COUNT OF RUNS (piClim-control, piClim-histaer)
CanESM5	Swart *et al.* (2019)	Cole *et al.* (2019b;c)	1, 3
HadGEM3-GC31-LL	Williams *et al.* (2018)	Andrews (2019; 2020)	1, 3
NorESM2-LM	Seland *et al.* (2020)	Oliviè *et al.* (2019a;b)	1, 3
MIROC6	Tatebe *et al.* (2019)	Sekiguchi and Shiogama (2019b;c)	1, 3

Table 2 Models used in the transient simulations (1850–2100) for this study.

average run of all models, the count of the ensemble members and the calendar type by each model are taken into account (see Appendix A for details).

2.2. AEROSOL RADIATIVE EFFECTS ESTIMATES

The ERF_{aer} is diagnosed as the difference of top-of-atmosphere (TOA) net radiative flux between the perturbed and control simulations, with climatological SSTs and sea ice distribution. The present-day ERF_{aer} is estimated from the 30-year (1850–1879) time slice simulation with piClim-aer configuration, which is evaluated against the reference baseline simulation (piClim-control). The estimated present-day ERF_{aer} has standard absolute errors of less than 0.1 W m^{-2} (Forster *et al.*, 2016). The aerosol loading and the consequent ERF_{aer} may also impact the AO, the leading mode of interannual atmospheric variability in the NH. Following Thompson and Wallace (2000), the AO is calculated based on the first mode of Empirical Orthogonal Function (EOF) analysis applied to monthly sea level pressure (SLP) anomalies during the winter months over the NH between 20°N and 90°N. The SLP field from the piClim-control simulation is used as the reference for computing SLP anomalies in all experiments and periods. Prior to the EOF analysis, the SLP anomalies are area-weighted by the square root of the cosine of latitude. The first EOF mode (EOF1) represents the characteristic spatial pattern of the AO, featuring opposite pressure anomalies between the Arctic and mid-latitudes. The corresponding normalized principal component (PC1) time series defines the AOI, which quantifies the strength and phase of the AO. The seasonal AOI is obtained by averaging the monthly AOIs over the winter months (DJF) and is used for the analysis.

The aerosols also may have a significant impact on the eddy-driven jet stream (EDJ) associated with the AO by altering its position. The position of the EDJ is obtained by employing an algorithm from Noyelle *et al.* (2022), in which the winter zonal wind over 925, 850, and 700 hPa between 15°N and 75°N are selected and vertically averaged, then the horizontal wind kinetic energy is calculated at every grid point. Subsequently, the latitudinal location of the maximum kinetic energy at every longitude is selected. A 25° rolling median is applied to the positions found in order to avoid any nonphysical detection of breaks in the jet. The 25° corresponds to 2000 km at 45°N, which is the typical size of mid-latitudes baroclinic disturbances (Hoskins and James, 2014). The calculated positions are averaged and then clustered with respect to the positive and negative phases of AO. The deviations in the average position of the jet stream between piClim-histaer and piClim-control will be analyzed in both of the AO phases. The analysis of extremes involves calculating the 90^{th} and 10^{th} percentile values of annual winter temperatures at each grid box for every period. The calculated percentiles in piClim-control are subtracted from those in every period to obtain their changes. The resulting anomalies in every AO phase are compared with each other by period.

The LRF is calculated using the radiative kernel method (Shell *et al.*, 2008; Soden and Held, 2006), by which a pre-computed radiative kernel is multiplied by the change in the atmospheric temperature profile between the analyzed period and piClim-control, and normalized by the change in mean SAT in the NH north of 20°N. The following formula describes the calculations of the feedback λ:

$$\lambda = \frac{\partial R}{\partial X}\frac{\Delta X}{\Delta \overline{T}_s} \quad (1)$$

The unit of λ is W m^{-2} K^{-1}. $\partial R/\partial X$ represents the radiative kernel with the same unit. $\Delta X/\Delta \overline{T}_s$ (K K^{-1}) represents the change in the temperature profile relative to the change in SAT mean of the NH domain between 20° and 90°N. The λ is integrated vertically over the troposphere from the surface to the tropopause, with the tropopause calculated following Feldl and Roe (2013) by setting it at 100 hPa at the equator and then interpolating it linearly following the latitudinal position to 300 hPa at the poles. Due to differing spatial resolutions between the model and the kernel, the model's dataset is regridded to match the kernel's resolution. The radiative kernel itself is estimated as the average of five kernels: GFDL AM2 (Soden *et al.*, 2008), ERAi (Huang *et al.*, 2017), CAM5 (Pendergrass *et al.*, 2018), HadGEM3-GA7.1 (Smith *et al.*, 2020b), and ERA5 (Huang and Huang, 2023a,b).

3. RESULTS

3.1. EFFECT OF PRESENT-DAY AEROSOLS ON THE ARCTIC CLIMATE

The ERF_{aer} under present-day conditions in the winter season (DJF) shows a positive forcing in the Arctic relative to pre-industrial conditions (Figure 1). The estimated average ERF_{aer} in the Arctic region, between 66°N and the North Pole, is approximately 0.14 W m^{-2} (Table A.2). This positive ERF_{aer} over the Arctic can be attributed to the increased aerosol load resulting from the transport of aerosols from lower latitudes (Figure A.1). The enhanced present-day aerosol loading, relative to pre-industrial levels (as of the year 1850), interacts with the dominant long wave (LW) radiation during the polar winter, effectively reducing the amount of outgoing LW radiation at the TOA, which leads to positive ERF_{aer} and consequent surface warming (Zhou and Savijärvi, 2014). In addition to the Arctic, the positive ERF_{aer} persists over the Sahara and large regions in central and northern Eurasia with high surface albedo. In contrast to most of the Arctic and other snow-covered areas, the present-day aerosol results in a negative ERF_{aer} over Greenland and the adjoining region. During winter, the primary pathway for aerosol transport to much of the Arctic, particularly the Eurasian sector, is through

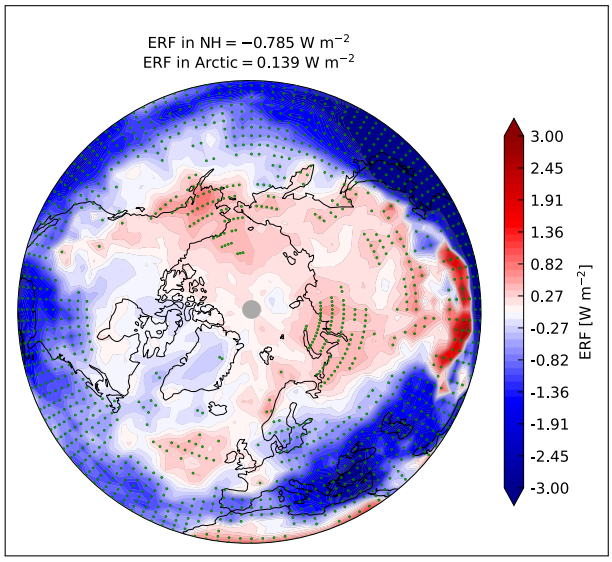

Figure 1 The present-day (2014) ERF_{aer} (W m^{-2}) in piClim-aer during the winter season (DJF) compared to the pre-industrial condition in piClim-control (1850) for the NH between 20°N and 90°N. The green dots refer to the statistical significance at a 75% confidence level, as determined by a t-test. The piClim-aer simulation is configured with present-day aerosols and fixed-SST, and piClim-control maintains forcing components at pre-industrial levels (1850). The figure shows the multi-model average of the nine models listed in Table 1.

low-level transport from Eurasia (Law *et al.*, 2014). However, this transport does not reach Greenland due to the positioning of the Arctic front and the prevailing transport from the North American region (Law *et al.*, 2014). In addition, the high elevation of Greenland limits the efficiency of low-level aerosol transport to its interior, as discussed by Guy *et al.* (2021). They showed that when air masses are advected from the coast and surrounding ocean and forced to ascend the elevated topography, orographic lifting induces adiabatic cooling, cloud formation, and precipitation, which together enhance aerosol removal through wet deposition. Consequently, aerosol concentrations over Greenland decrease during such upslope flow events, particularly under anomalous cyclonic circulation over southeast Greenland, which occurs more frequently in winter (Guy *et al.*, 2021; Schuenemann *et al.*, 2009). At lower latitudes, the negative ERF_{aer} is more dominant, with the average ERF_{aer} in the NH between 20°N and 66°N being approximately –0.91 W m^{-2} (Table A.3). Overall, the mean ERF_{aer} for the NH domain from 20°N to 90°N is approximately –0.79 W m^{-2} (Table A.1), reflecting the significantly larger magnitude of the negative forcing at mid- and low latitudes relative to the positive forcing in the Arctic (Figure 1).

The increase in atmospheric aerosols over the NH and its impact on the ERF have, in turn, modified the AO (Figure 2). It shows significant positive SLP anomalies in the Arctic region, which extend even into northern North America. In contrast, negative SLP anomalies are prevalent in the northern Atlantic, northern Pacific, most

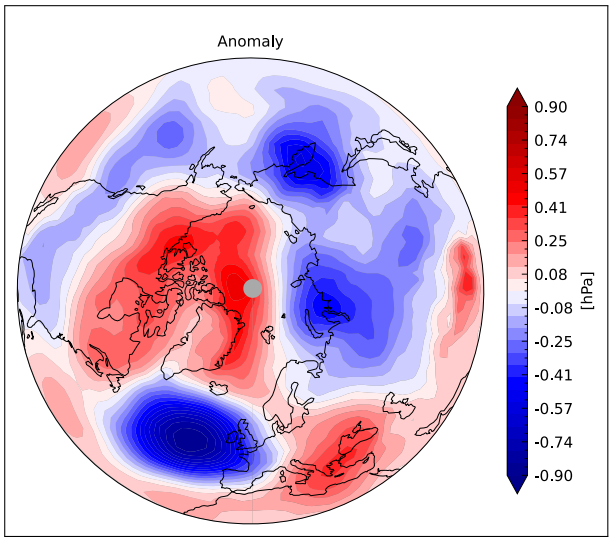

Figure 2 Leading empirical orthogonal functions (EOF) of the winter (DJF) mean SLP (hPa) anomalies for piClim-aer (2014) compared to the pre-industrial condition in piClim-control (1850) for the NH between 20°N and 90°N. The piClim-aer simulation is configured with present-day aerosols and fixed-SST, and piClim-control maintains forcing components at pre-industrial levels (1850).

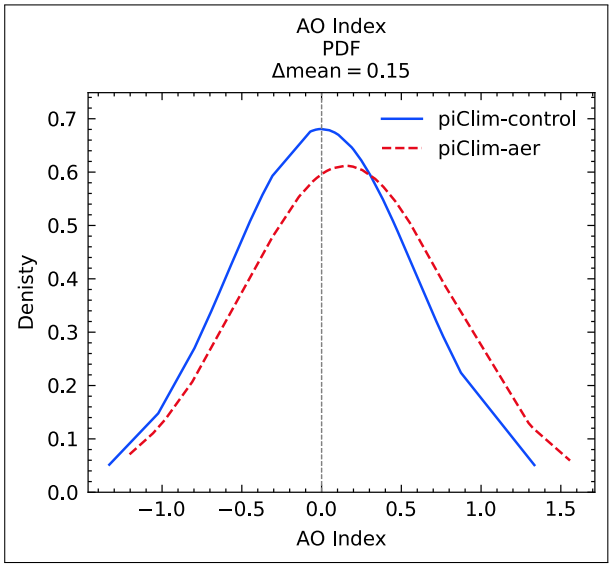

Figure 3 Comparison of probability density function (PDF) of AOI for the piClim-control and piClim-aer during the winter (DJF). Both simulations cover a 30-year period. In piClim-aer, present-day (2014) aerosols are applied with fixed-SST, whereas piClim-control maintains all forcing components at pre-industrial levels (1850). By each simulation, the multi-model mean SLP is first calculated, and the AOI and its corresponding PDF are derived from this multi-model mean SLP.

of the United States, and north and central Eurasia. These changes in SLP result in a positive anomaly in AOI in piClim-aer compared to piClim-control (Figure 3). Similar findings were reported by Zanis *et al.* (2020), who demonstrated that aerosol-induced circulation changes exhibit a characteristic dipole pattern, characterized by the intensification of the Icelandic low and an anticyclonic anomaly over southeastern Europe.

3.2. TRANSIENT EFFECT OF AEROSOLS

3.2.1. Aerosol loading and its impact on radiative forcing

The temporal variation of the mean aerosol optical depth (AOD) in NH (20°N–90°N) during the winter is illustrated in Figure 4a. The AOD has shown an increasing trend since 1850, peaking in the second half of the 20th century (AOD ≈ 0.15). Later, it decreases toward the end of the 21st century (AOD ≈ 0.1). The ERF_{aer} also shows a similar pattern, increasing from 1850 toward the end of the 21st century (Figure 4b). A negative ERF_{aer} indicates that aerosol loading in the NH results in net cooling at TOA. This increase in aerosol-induced cooling is reversed in the second half of the 20th century due to the reduction in aerosol concentrations (Figure 4a and b). The most significant changes in ERF_{aer} occurred between 1970 and 1980, contributing to an increase in the upward SW radiation at TOA (Figure A.2a), which also peaks at the same time and exceeds 1.5 W m^{-2}. Meanwhile, upward LW radiation at TOA shows negative anomalies on average between 1900 and 2050, reaching a maximum reduction of approximately 0.7 W m^{-2} between 1970 and 1980 (Figure A.2b), corresponding to a positive radiative forcing. However, this reduction in LW radiation does not offset the contribution from increased SW radiation in the context of net negative ERF_{aer}.

Likewise, in the Arctic region (66°N to 90°N), changes in AOD are qualitatively similar to those observed in the NH. There was a significant increase in aerosol burden between 1970 and 1980, indicating enhanced aerosol transport to the Arctic region (Figure 4c). The ERF_{aer} in the Arctic fluctuates between positive and negative values, as depicted in Figure 4d. However, the 30-year moving average demonstrates that the ERF_{aer} has been negative since 1920, reaching its lowest point between 1970 and 1980, in line with the AOD trends. Unlike the ERF_{aer} in the NH, the variation in the winter ERF_{aer} over the Arctic is mainly influenced by changes in the upward LW (Figure A.3b), which are stronger in magnitude than the changes in upward SW (Figure A.3a), highlighting the key role of LW radiative processes in modulating the Arctic energy budget in response to aerosol forcing. The negative ERF_{aer} and increased outgoing LW flux at TOA indicate a net cooling at TOA, but do not directly describe surface temperature changes. Due to aerosol-induced modifications of the AO and LRF, energy can be redistributed within the Arctic column, and surface warming in winter can coexist with negative ERF and increased outgoing LW flux at TOA, as shown later in Sections 3.2.2. and 3.3.

The above analysis highlights the significant role that aerosols play in the Arctic climate and its variability. However, our understanding of how sensitive the changes in the Arctic climate are to aerosols is still limited. For this, we have examined periods of low and high aerosol loading based on transient simulations. The

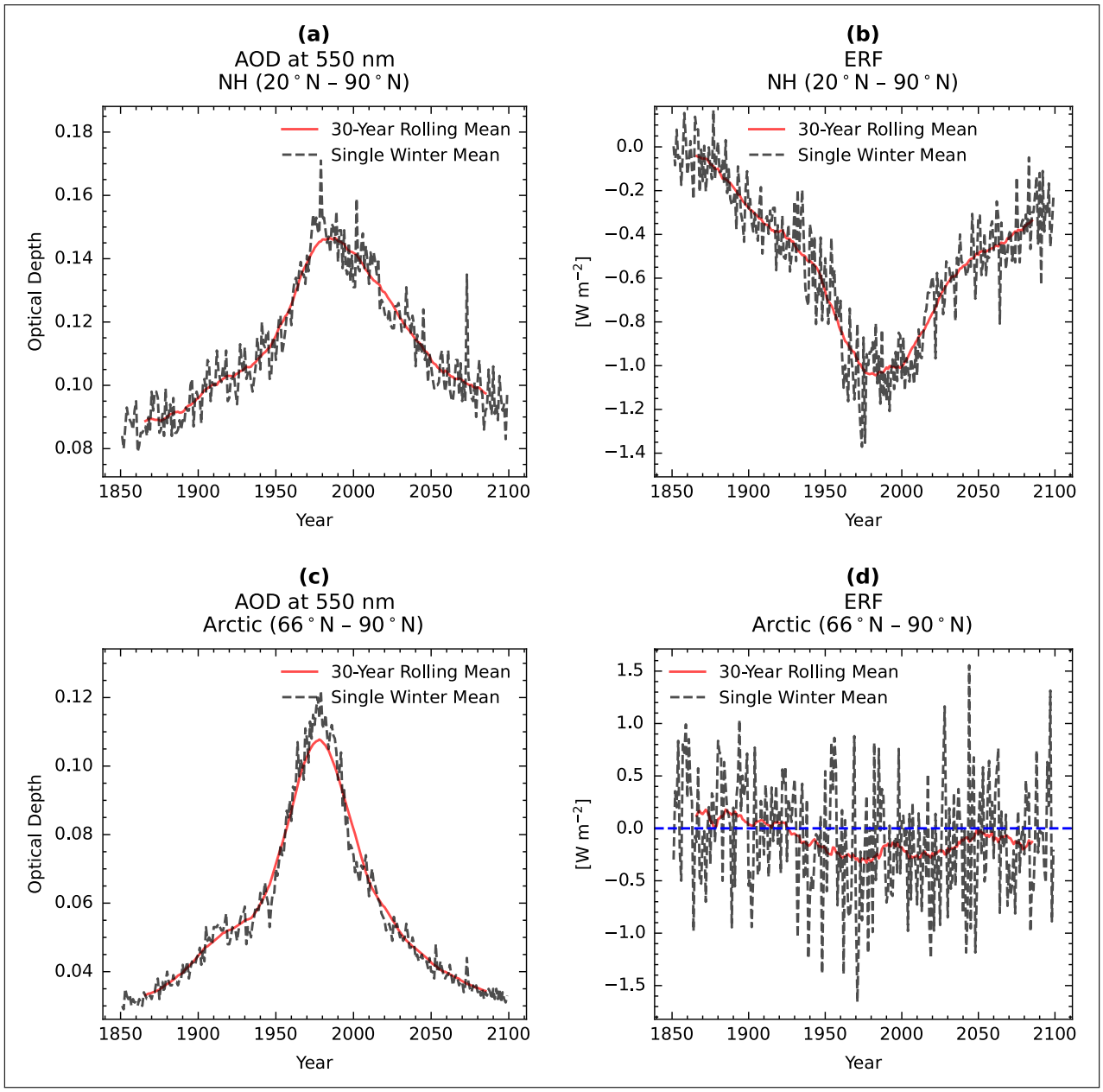

Figure 4 Time series of **(a, b)** aerosol optical depth at 550 nm and **(c, d)** ERF_{aer} (W m^{-2}) during winter (DJF) from the piClim-histaer transient simulation (1851–2099), shown for the NH between 20°N and 90°N (a, c), and the Arctic region between 66°N and 90°N (b, d). The dashed black lines are for single winter means, the red solid lines refer to the 30-year moving average of winter means, and the blue dashed line indicates the zero value. The both figures show the multi-model average of the four models listed in Table 2.

temporal distribution of AOD in the transient simulations indicates a peak between 1965 and 2014, specifically around 1988, while showing minimal AOD loading between 1851 and 1900 (50 years each). We have therefore designated these periods as high and low aerosol loading scenarios, respectively, to examine the aerosol sensitivity to the Arctic climate.

While it may be tempting to simplify the analysis by comparing only the pre-industrial conditions represented by the piClim-control (1850) with the high-aerosol period (1965–2014), our choice to include the early industrial low-aerosol period (1851–1900) is deliberate. This interval captures the initial rise in anthropogenic aerosol emissions while still representing a period of relatively low aerosol concentrations. Including it enables us to assess how the Arctic responds to any changes in aerosol loading. It also gives us an intermediate forcing level, allowing us to see how the Arctic responds to incremental changes, not only to the most substantial aerosol forcing. This approach allows us to examine whether the climate response increases linearly, slows down, levels off, or even reverses beyond certain forcing thresholds—insights that would be missed by comparing only zero versus maximal forcing. In this way, the early industrial period provides an informative 'middle ground' that strengthens the robustness of our sensitivity estimates and enhances our understanding of aerosol-climate interactions in the Arctic.

3.2.2. Aerosol-sensitivity of Arctic Oscillation (AO)

Figure 5 illustrates the distribution of the AOI for high and low aerosol loading scenarios. The figure shows that the AOI distribution is positively skewed compared to piClim-control for both aerosol conditions. This skewness suggests a relative decrease in SLP over the Arctic and an increase in mid-latitude SLP. The positively skewed AOI distribution indicates a stronger polar vortex and a more stable jet stream, which reduces the frequency and intensity of Arctic air incursions into mid-latitudes (Limpasuvan and Hartmann, 2000), suggesting a substantial aerosol impact on the Arctic climate. However, the sensitivity of the AOI to aerosols shows less influence on the extreme AOI distributions (90th and 10th percentile). The variability in the AOI induced by aerosols suggests that aerosol forcing could moderate AOI variability, resulting in a more constrained range of AO patterns. This has important implications for winter climate variability in the NH. From the AOI distribution, the estimated AOI anomaly illustrates that the anomaly is larger (0.25) for the low aerosol conditions compared to the high aerosol scenario, which has an anomaly of 0.1. This suggests that changes in the AO are driven by varying aerosol concentrations, leading to significant effects on both regional and global climates despite the magnitude of the sensitivity to aerosols.

A marked difference is evident between the AOI probability density functions (PDFs) during the piClim-histaer periods (Figure 5) and the AOI PDF in piClim-aer (Figure 3). This difference primarily arises from how aerosol forcing is represented in the two simulations. piClim-aer uses fixed present-day aerosol concentrations (as of 2014) throughout the simulation. This idealized setup imposes a steady radiative forcing, so the atmosphere settles into a relatively stable circulation response. In contrast, piClim-histaer includes the historical evolution of aerosols, capturing the rise and fall of aerosol emissions over time, which drives stronger variability in AO and thus changes the AOI distribution more.

Figure 6 illustrates the SAT anomalies for the low and high aerosol loading scenarios. The magnitude of temperature changes across the NH varies between periods. In both cases, an increase in the SAT is noticed over Eurasia and western North America, while temperatures mainly decrease in most lower latitude regions. Notably, in the high aerosol scenario, SAT warming is concentrated in the Arctic region, with temperature increases of up to approximately 1 K. However, warming in the Arctic region is less dominant in the low aerosol scenario. Importantly, the strong warming is localized over the Arctic in the high-aerosol scenario, creating a pronounced temperature gradient toward the lower latitudes. The profound changes in the Arctic and associated climate variability (AO) are also accompanied by variations in extreme weather events in the mid-latitudes, as extreme weather events are typically linked to the phase of the AO. Figure 7 illustrates the aerosol sensitivity to extreme SAT (90th and 10th percentile) during the positive AO phase. During this positive AO phase, the 10th percentile of the SAT anomaly shows positive values over most of the NH for

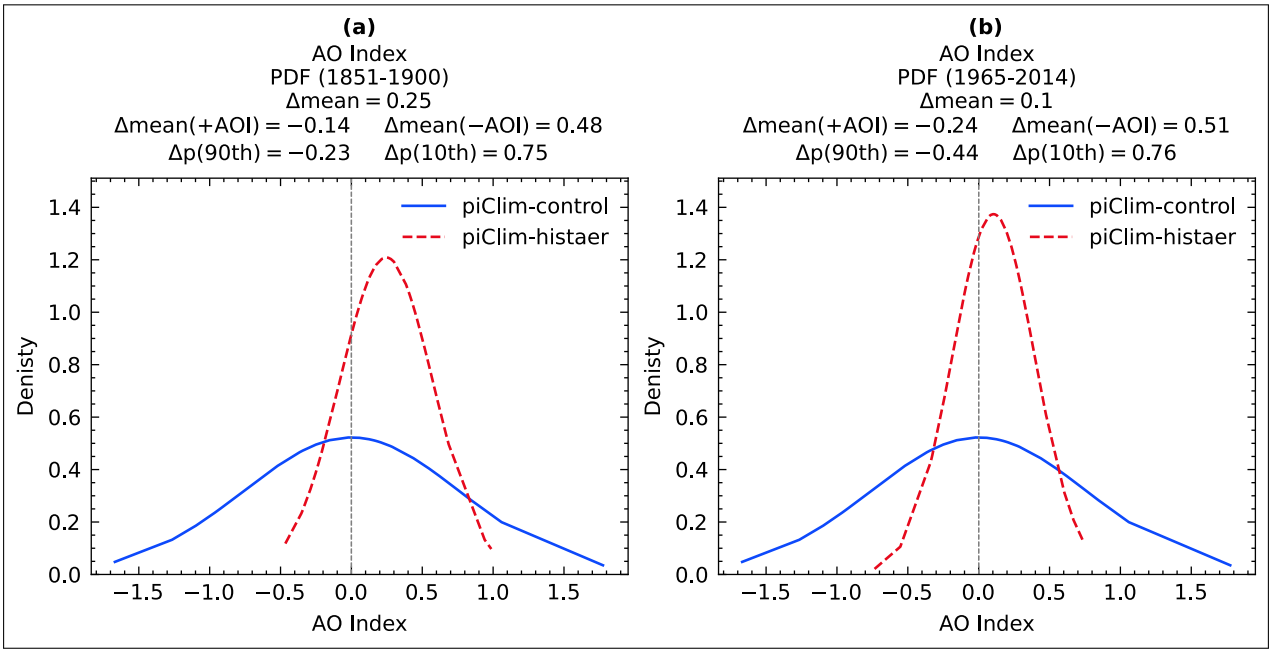

Figure 5 Comparison of PDF of AOI for the piClim-control and piClim-histaer during the winter (DJF). PDF for **(a)** low aerosol loading scenario (1851–1900) and **(b)** high aerosol burden (1965–2014), respectively. Δ*mean* refers to the anomaly of the average AOI in piClim-histaer's period from the average piClim-control. Δ*mean*(*+AOI*) and Δ*mean*(*–AOI*) refer to the anomalies of the average positive and negative index values respectively.

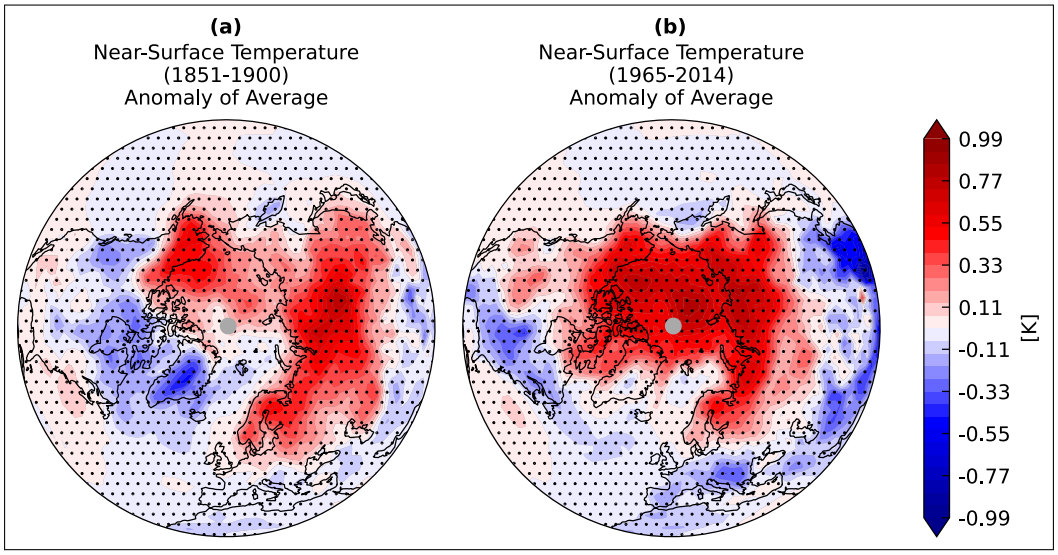

Figure 6 Comparison of SAT (K) anomaly relative to piClim-control during the winter (DJF) for **(a)** low aerosol loading scenario (1851–1900) and **(b)** high aerosol burden (1965–2014), respectively. The black dots indicate the statistical significance at a 75% confidence level.

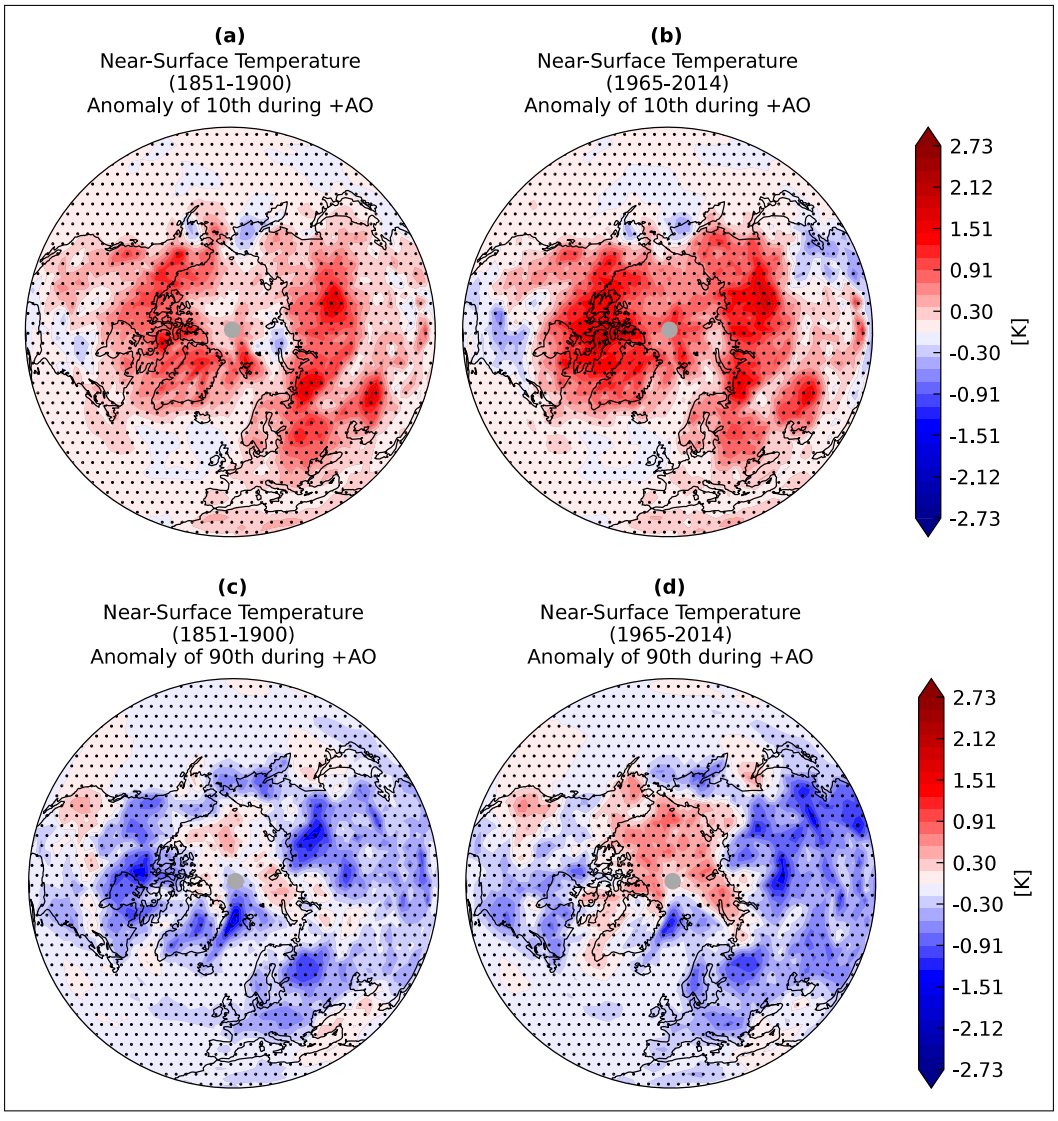

Figure 7 Comparison of 10^{th} and 90^{th} percentiles of SAT (K) anomaly relative to piClim-control during the winter (DJF) for positive AO phase. Panels **(a)** and **(b)** show the 10^{th} percentile of SAT anomaly for low aerosol loading scenario (1851–1900) and high aerosol scenario (1965–2014), respectively. Panels **(c)** and **(d)** show the 90^{th} percentile of SAT anomalies for the same two scenarios. The black dots indicate the statistical significance at a 75% confidence level.

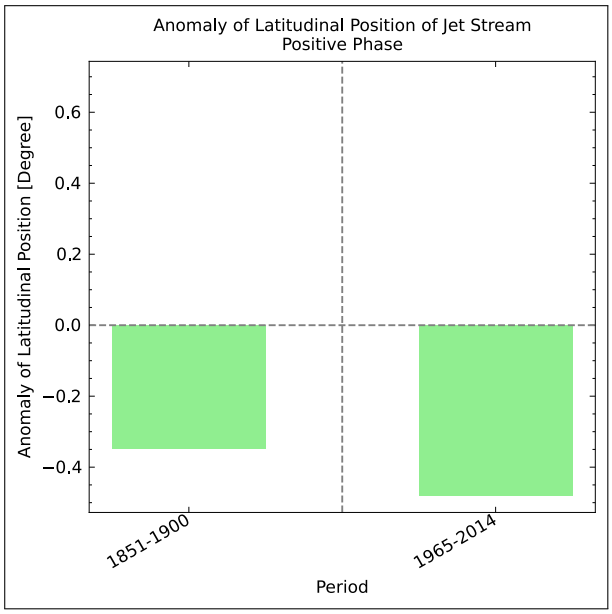

Figure 8 Anomalies of the latitudinal position of the jet stream in piClim-histaer during the positive AO with respect to piClim-control. The periods 1851–1900 and 1965–2014 represent low and high aerosol loading scenarios, respectively.

both low and high aerosol loading scenarios (Figure 7a and b). It indicates that the aerosol enhancement leads to less extreme cold winters. This less extreme cold winter is more pronounced in the high aerosol loading scenario, especially over the Arctic, compared to the low aerosol scenario. On the other hand, the anomalies of the 90th percentile of annual winter temperatures are negative across most of the NH in both periods (Figure 7c and d), except for the Arctic. From the figure, it is seen that there is a strong aerosol sensitivity to Arctic warming, indicating that enhanced aerosol loading in the high aerosol scenario results in strong positive SAT anomalies (90th percentile), particularly in the Arctic region, where extreme SAT has increased by up to 1.5 K. It suggests that aerosol enhancement leads to warmer winters in the Arctic. Furthermore, the significant changes in the SAT and AO also affect the position of jet streams, which influences the storm tracks and the magnitude and intensity of cold/warm air spells. Figure 8 illustrates the latitudinal position of the jet stream during the positive AO phase and its relation to the aerosol enhancement. During the positive AO phase, the jet stream shifted southerly, with the most significant shifts occurring in the high aerosol scenario. This southern shift of the jet stream during the positive AO phase reflects the weakened positive phase, with moderate impacts associated with the AO on the climate of mid-latitudes.

Similarly, during the negative AO phase, 10th percentile SAT anomalies are positive over the NH, irrespective of the aerosol loading scenario. However, the magnitudes of these anomalies do not significantly differ between the two periods (Figure 9a and b), unlike the variations seen in the positive AO phase. In addition, some negative SAT anomalies are observed over Greenland, western North America, and the Mediterranean in the low aerosol scenario. Conversely, the anomalies of the 90th percentile of annual winter temperatures are negative over most of the NH during both periods (Figure 9c and d). However, positive SAT anomalies appear in parts of Eurasia and the Arctic during the high aerosol scenario, similar to that observed in the positive AO phase. Moreover, during the negative AO phase, the position of the jet stream has been shifted northward in both low and high aerosol scenarios (Figure 10). It is important to note that aerosol enhancement is less sensitive to this northward shift of the jet stream.

3.3. AEROSOL-SENSITIVITY OF LAPSE RATE FEEDBACK (LRF)

In the Arctic, the vertically non-uniform warming of the troposphere results in a positive LRF, which has been identified as the contributor to Arctic amplification. The above analysis indicates that increased aerosol concentration significantly warms the Arctic. Likewise, the LRF is also sensitive to aerosol enhancement. Figure 11 illustrates the spatial distribution of LRF for low and high aerosol scenarios. In the high aerosol scenario, a strong positive LRF is observed over the Arctic and the adjoining regions, specifically over northern Eurasia and northern North America. In contrast, during the low aerosol scenario, a strong positive LRF appears only in a few regions of northern Eurasia and northwest North America. In the Arctic, the pronounced positive LRF correlates with the enhancement of aerosol loading. Conversely, during the high aerosol scenario, negative feedback affects a broader area across the continents at lower latitudes, showing higher absolute values compared to the low aerosol scenario. The positive LRF over the Arctic can be attributed to a greater warming near the surface compared to the upper troposphere, as illustrated in Figure 12. This warming has intensified during the high aerosol scenario, likely due to increased aerosol loading that reduces outgoing LW radiation during the polar night, trapping more heat near the surface. In contrast, the negative LRF at lower latitudes is associated with warming the upper troposphere that exceeds the relatively limited surface warming in some regions and even contrasts with surface cooling in others (Figure 12).

4. SUMMARY AND CONCLUSIONS

We conducted a comprehensive analysis of the impact of aerosol forcing on the Arctic climate during the winter, utilizing data from CMIP6 models. The study focuses on understanding the role of aerosols in Arctic warming/cooling and its consequences on the Arctic

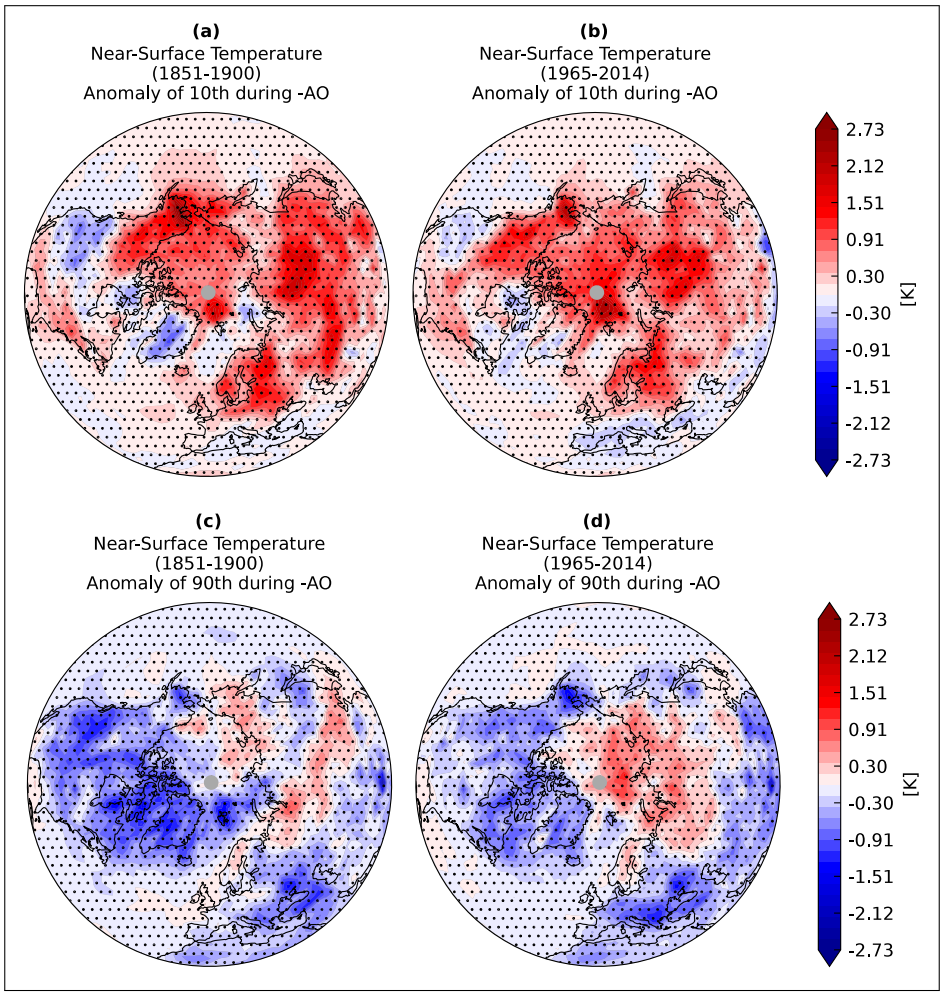

Figure 9 Comparison of 10th and 90th percentiles of SAT (K) anomaly relative to piClim-control during the winter (DJF) for negative AO phase. Panels **(a)** and **(b)** show the 10th percentile of SAT anomaly for low aerosol loading scenario (1851–1900) and high aerosol scenario (1965–2014), respectively. Panels **(c)** and **(d)** show the 90th percentile of SAT anomalies for the same two scenarios. The black dots indicate the statistical significance at a 75% confidence level.

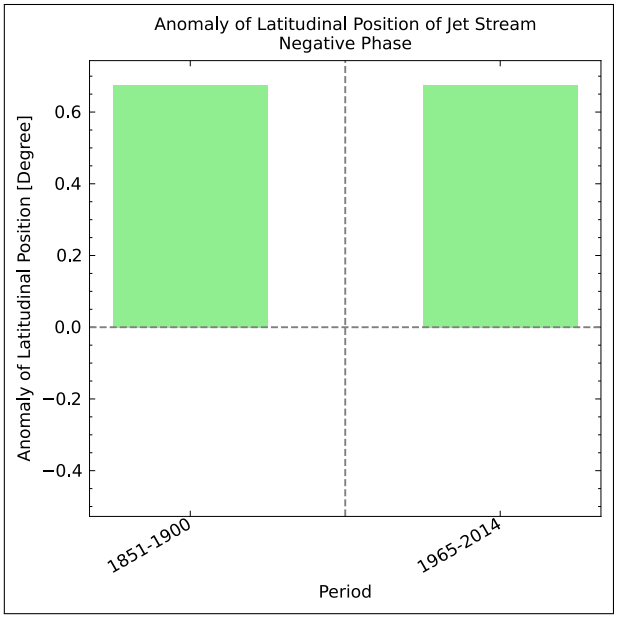

Figure 10 Anomalies of the latitudinal position of the jet stream in piClim-histaer during the negative AO with respect to piClim-control. The periods 1851–1900 and 1965–2014 represent low and high aerosol loading scenarios, respectively.

climate variability, specifically AO. The study also delved into how aerosol transport into the Arctic region affects the LRF.

The present-day aerosol induces a positive ERF_{aer}, particularly in the Arctic, compared to pre-industrial conditions during winter (DJF). The estimated average ERF_{aer} in the Arctic region is approximately 0.14 W m^{-2}, which is linked to enhanced aerosol loading resulting from strong transport from Eurasia and adjoining regions. This enhanced aerosol loading reduces the amount of outgoing LW radiation at the TOA, causing positive ERF_{aer} and warming in the region. However, a significant negative ERF_{aer} of approximately –0.91 W m^{-2} is simulated at lower latitudes (between 20°N and 66°N) due to an increase in upward SW radiation caused by aerosol reflection. Furthermore, our analysis suggests that the enhanced aerosol loading and subsequent warming in the Arctic have a considerable impact on the AO. The positive aerosol ERF_{aer} leads to significant positive SLP anomalies over the Arctic, which extend into northern North America, while negative SLP anomalies dominate in other parts of the NH.

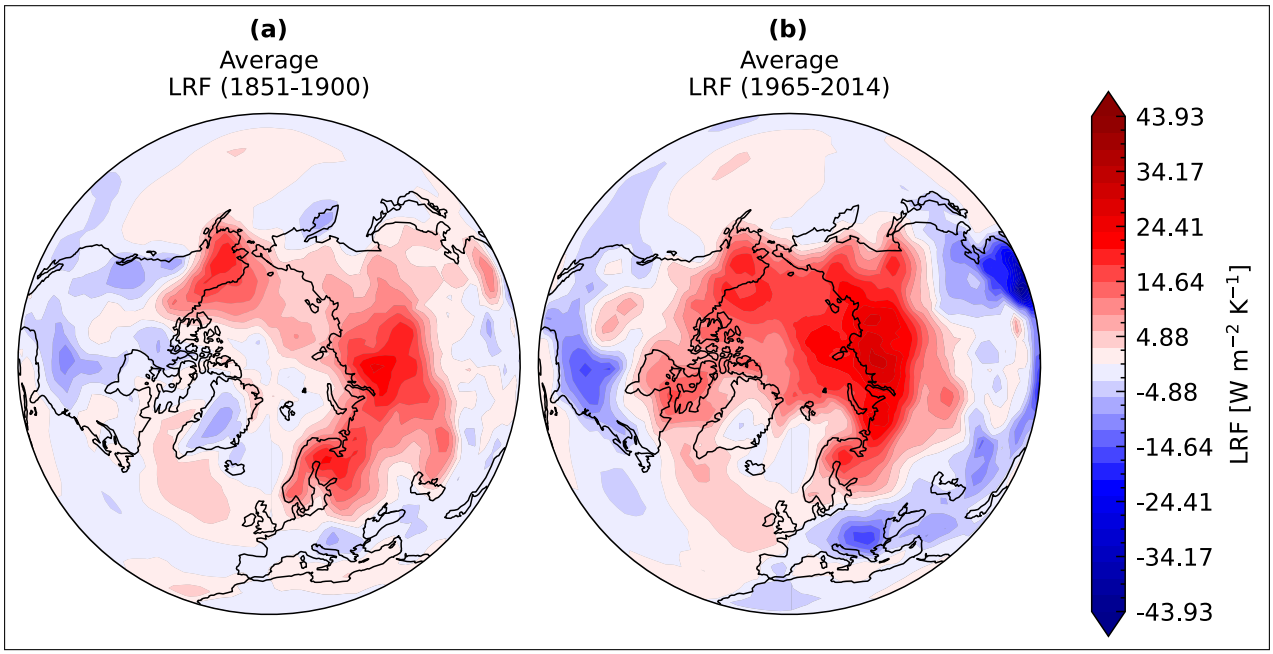

Figure 11 Comparison of the LRF (W m^{-2} K^{-1}) in the NH (between 20°N and 90°N) during **(a)** low aerosol loading scenario (1851–1900) and **(b)** high aerosol scenario (1965–2014) for the winter (DJF).

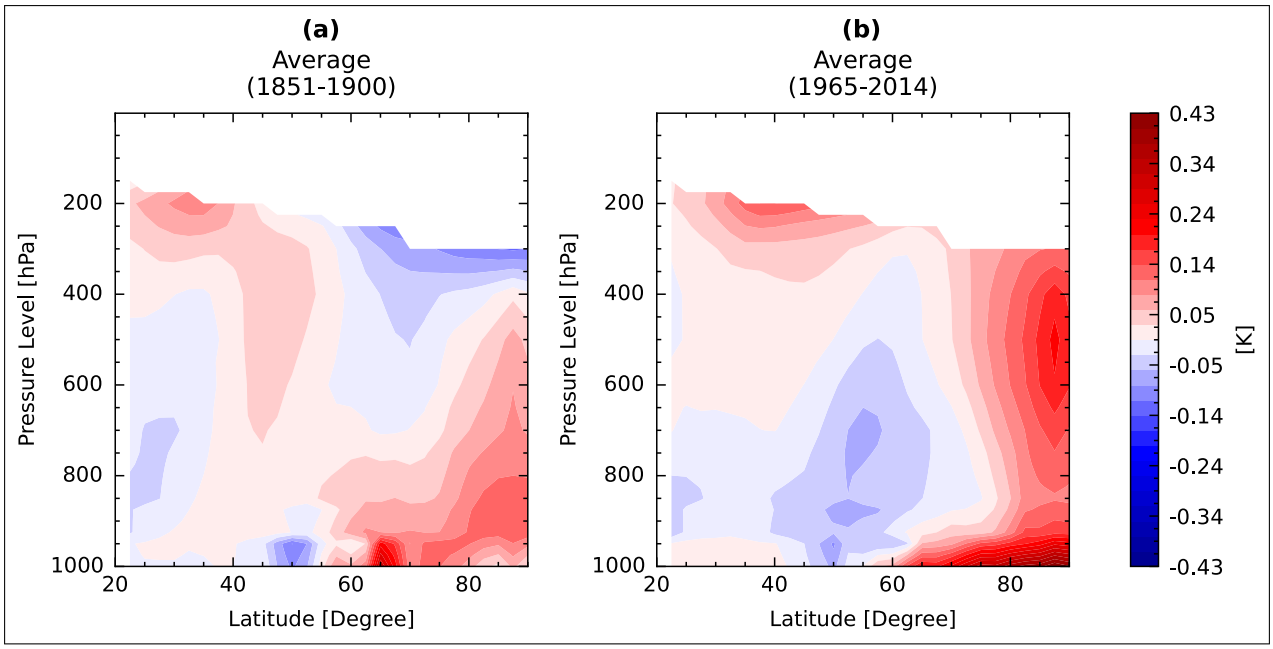

Figure 12 The latitudinal cross-section of the winter (DJF) temperature anomalies (K) relative to piClim-control in the NH (between 20°N and 90°N) during **(a)** low aerosol loading scenario (1851–1900) and **(b)** high aerosol scenario (1965–2014).

Importantly, the increase in aerosols has resulted in a positively skewed distribution of the AOI compared to the control simulation (piClim-control).

Similar to the present-day ERF_{aer}, the transient simulations also demonstrate a significant impact on the ERF_{aer}. However, aerosol concentrations exhibit considerable global and temporal variability. In the NH, the aerosol concentrations were at their lowest between 1850 and 1900. They then increased over time, peaking between 1964 and 2014, before declining to their minimum levels by the end of the century. Thus, to assess the sensitivity of aerosol loading in the Arctic climate, we compared periods of low and high aerosol emissions, specifically within the NH. During the high aerosol scenario, the SAT warming is concentrated in the Arctic region with a magnitude of anomaly up to ≈ 1 K from the pre-industrial conditions. In contrast, the Arctic is less affected by warming during the low aerosol scenario. In both low- and high-emission scenarios, the AOI distribution is positively skewed, indicating that variations in aerosol concentrations drive changes in the AO, leading to a predominance of its positive phase,

which indicates a strengthened polar vortex and a more stable jet stream. However, the AOI distribution is less sensitive to the enhancement of aerosols. Consequently, the increased aerosol loading and its relationship to the AO may contribute to fluctuations in extreme weather. Our analysis indicates that aerosol enhancement results in extremely warm winters in the Arctic, in contrast to most of the NH, irrespective of the phase of the AO. Additionally, during the positive AO phase, the enhancement of aerosols causes the jet stream to shift southward, while it moves northward during the negative AO phase.

Furthermore, the positive LRF arises from the vertically non-uniform warming of the troposphere, which contributes to the amplification of the Arctic SAT. Our analysis indicates that aerosol enhancement leads to an increase in positive LRF in the Arctic. The enhanced positive LRF over the Arctic can be attributed to more significant warming near the surface compared to the upper troposphere, which is associated with the high aerosol scenario.

Our analysis suggests that aerosol loading has a substantial effect on the Arctic climate. Specifically, the present-day aerosol loading over the Arctic leads to a positive ERF_{aer}, implying surface warming during winter (DJF). Furthermore, aerosol-induced warming in the Arctic region also affects climate variability, especially the AO. The LRF, which acts as a positive feedback in the Arctic and plays a crucial role in Arctic amplification by enhancing SAT responses to radiative forcing under human-induced climate change, is further influenced by aerosol enhancement. However, the quantification and future projections of the effect of aerosols on the Arctic climate remain highly uncertain due to the spatial and temporal variability of aerosols. A better understanding of the ERF_{aer} is essential for constraining the impact of aerosols on the Arctic climate and its associated variability, including the AO and related impacts, such as climate extremes. Furthermore, future studies could extend this work by exploring the indirect effects of aerosol-cloud interactions, which may further modulate the Arctic energy balance and feedback processes.

APPENDIX A: METHODS OF CALCULATIONS

A1. MULTI-MODEL AVERAGES

To ensure consistency in the evaluation of the multi-model mean of any variable (e.g., ERF, AOD, SAT), both the ensemble size and calendar type of each model were taken into consideration. Since we used an equal number of ensemble members for all models in each experiment, no ensemble-size weighting was necessary. However, the models used different calendar systems (e.g., Gregorian, 360-day, or no-leap calendars), which led to varying month lengths. To address this, all monthly means were weighted according to the number of days in the corresponding month of each model before calculating the average.

The monthly weighted mean for each variable V across n models was computed using the following formula:

$$V_{\text{Average}} = \frac{\sum_{i=1}^{n} V_i L_i}{\sum_{i=1}^{n} L_i} \tag{A1}$$

where:

V_i is the variable value from model i

L_i is the count of days in the given month for model i

Prior to averaging, all model outputs were regridded to a common spatial resolution using bilinear interpolation. The common resolution was chosen to match the coarsest horizontal resolution among the models to avoid artificial enhancement of spatial detail.

A2. SEASONAL AND PERIOD MEANS

For the calculation of winter season averages (DJF), each month was weighted by the number of days in that month. Due to the structure of the DJF season spanning across calendar years, data from January and February of the first simulation year were excluded, as the complete winter season average could not be calculated for that year. Therefore, winter averages begin with the second year of each period analyzed.

The monthly lengths used in the multi-model average were computed as the mean of month lengths across all models. These lengths were then used in the calculation of seasonal and periods' means of any variable across the average run.

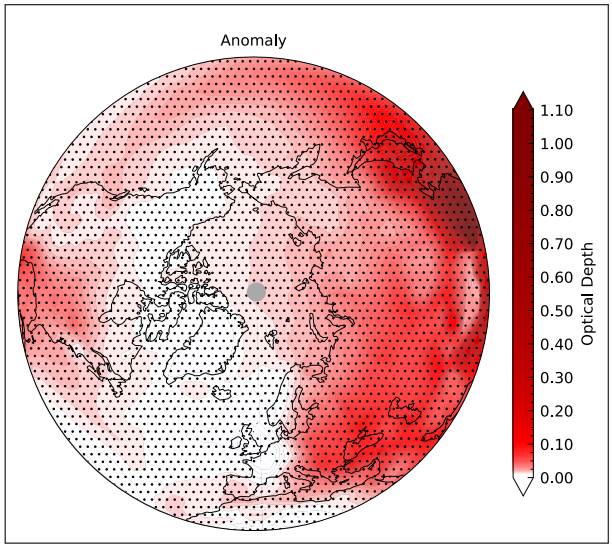

Figure A.1 Aerosol optical depth (AOD) anomalies in piClim-aer from piClim-control over the NH between 20°N and 90°N during the winter (DJF). The black dots indicate where the AOD difference between piClim-control and piClim-aer is statistically significant at a 75% confidence level.

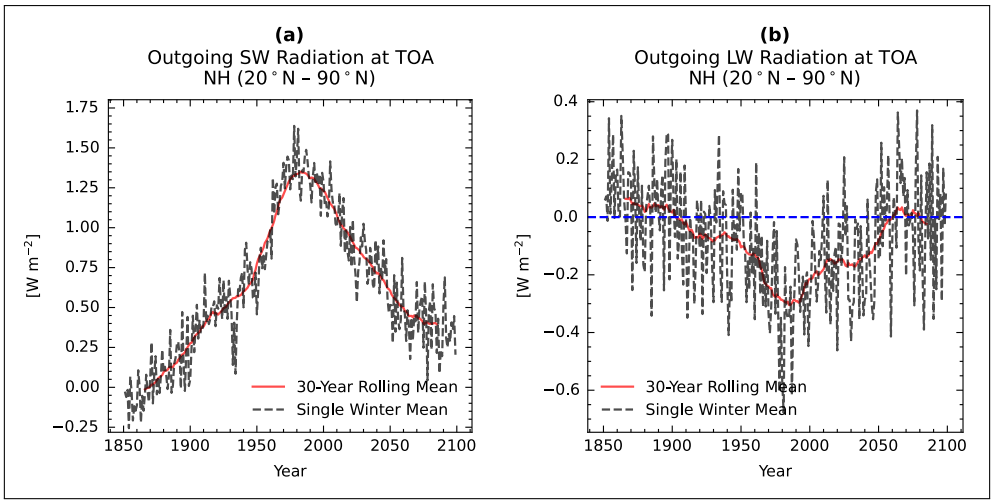

Figure A.2 Time series of anomalies of **(a)** outgoing SW radiation at TOA and **(b)** outgoing LW radiation at TOA (in W m^{-2}) in piClim-histaer from piClim-control for winter (DJF). The dashed black lines are for single winter means, and the red solid lines refer to the 30-year moving average of winter means, and the blue dashed line indicates the zero value. The values are for the NH between 20°N and 90°N from 1851 to 2099.

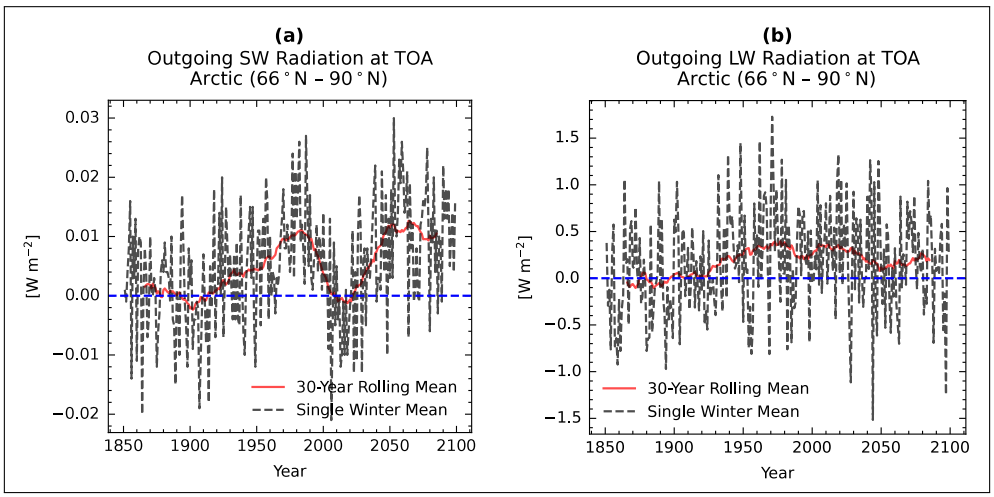

Figure A.3 Time series of anomalies of **(a)** outgoing SW radiation at TOA and **(b)** outgoing LW radiation at TOA (in W m^{-2}) in piClim-histaer from piClim-control for winter (DJF). The dashed black lines are for single winter means, the red solid lines refer to the 30-year moving average of winter means, and the blue dashed line indicates the zero value. The values are for the Arctic between 66°N and 90°N from 1851 to 2099.

MODELS	ERF_{aer}	CHANGE OF UPWARD SW RADIATION AT TOA	CHANGE OF UPWARD LW RADIATION AT TOA
CNRM-CM6-1	−1.168	1.255	−0.09
CNRM-ESM2-1	−0.502	0.89	−0.391
CanESM5	−0.432	0.441	−0.008
EC-Earth3	−0.398	0.55	−0.15
IPSL-CM6A-LR-INCA	−0.562	0.498	0.058
MIROC6	−0.715	1.104	−0.394
MPI-ESM-1-2-HAM	−1.358	1.496	−0.135
MRI-ESM2-0	−1.055	1.915	−0.857
UKESM1-0-LL	−0.753	0.929	−0.176
Multi-Model Average	**−0.785**	**1.024**	**−0.24**

Table A.1 ERF_{aer} and its solar and terrestrial components over the NH domain between 20°N and 90°N as derived from the time-slice simulations (piClim-aer) relative to the reference simulations (piClim-control). Units are in W m^{-2}.

MODELS	ERF_{aer}	CHANGE OF UPWARD SW RADIATION AT TOA	CHANGE OF UPWARD LW RADIATION AT TOA
CNRM-CM6-1	0.07	0.015	−0.084
CNRM-ESM2-1	0.593	−0.005	−0.588
CanESM5	0.046	−0.057	0.011
EC-Earth3	0.695	0.004	−0.697
IPSL-CM6A-LR-INCA	1.148	0.027	−1.177
MIROC6	0.422	0.012	−0.435
MPI-ESM-1-2-HAM	−0.078	−0.026	0.106
MRI-ESM2-0	−0.806	0.002	0.806
UKESM1-0-LL	−0.863	−0.007	0.87
Multi-Model Average	**0.139**	**−0.004**	**−0.134**

Table A.2 ERF_{aer} and its solar and terrestrial components over the Arctic between 66°N and 90°N as derived from the time-slice simulations (piClim-aer) relative to the reference simulations (piClim-control). Units are in W m^{-2}.

MODELS	ERF_{aer}	CHANGE OF UPWARD SW RADIATION AT TOA	CHANGE OF UPWARD LW RADIATION AT TOA
CNRM-CM6-1	−1.356	1.444	−0.091
CNRM-ESM2-1	−0.669	1.026	−0.361
CanESM5	−0.497	0.508	−0.011
EC-Earth3	−0.566	0.634	−0.066
IPSL-CM6A-LR-INCA	−0.805	0.565	0.233
MIROC6	−0.887	1.27	−0.388
MPI-ESM-1-2-HAM	−1.568	1.746	−0.175
MRI-ESM2-0	−1.093	2.201	−1.106
UKESM1-0-LL	−0.737	1.067	−0.331
Multi-Model Average	**−0.911**	**1.164**	**−0.255**

Table A.3 ERF_{aer} and its solar and terrestrial components over the NH domain outside the Arctic (i.e., between 20°N and 66°N) as derived from the time-slice simulations (piClim-aer) relative to the reference simulations (piClim-control). Units are in W m^{-2}.

DATA ACCESSIBILITY STATEMENT

All CMIP6 RFMIP model data used in this study were obtained from the Earth System Grid Federation (ESGF, https://esgf.llnl.gov/). The variables analyzed include: psl, tas, ta, rsdt, rsut, rlut, ua, and va. Radiative kernel datasets were obtained from Huang, Han; Huang, Yi (2023a), Data for ERA5 radiative kernels, Mendeley Data, V4, doi: 10.17632/vmg3s67568.4, available at https://data.mendeley.com/datasets/vmg3s67568/4. Processed datasets generated in this study are available from the corresponding author upon reasonable request.

CODE AVAILABILITY STATEMENT

The analysis and plotting code used in this study is available from the corresponding author upon reasonable request.

ACKNOWLEDGEMENTS

We acknowledge the World Climate Research Programme, which, through its Working Group on Coupled Modelling, coordinated and promoted CMIP6. We thank the climate modeling groups for producing and making available their model output, the Earth System Grid Federation (ESGF) for archiving the data and providing access, and the multiple funding agencies who support CMIP6 and ESGF.

We further acknowledge the developers of the radiative kernel datasets used in this study, including GFDL AM2, ERA-Interim, CAM5, HadGEM3-GA7.1, and ERA5, and thank them for making these datasets publicly available. We also thank the anonymous reviewers for their valuable comments on an earlier version of this manuscript.

FUNDING INFORMATION

This research has been supported by the Deutsche Forschungsgemeinschaft (DFG, German Research Foundation; grant no. 268020496 – TRR 172) within the Transregional Collaborative Research Centre 'Arctic Amplification: Climate-Relevant Atmospheric and Surface Processes and Feedback Mechanisms (AC)[3]'.

COMPETING INTERESTS

The authors have no competing interests to declare.

AUTHOR CONTRIBUTIONS

K.A. designed the study, performed the calculations and plotting, conducted the analysis, and drafted the manuscript. S.D. supervised the work and contributed to the analysis, writing and revising the manuscript. All other authors provided comments and contributed to revising the manuscript.

AUTHOR AFFILIATIONS

Khaled Al Hajjar orcid.org/0009-0009-8611-807X
Institute for Meteorology, Leipzig University, Leipzig, Germany

Sudhaker Dipu orcid.org/0000-0003-4514-8968
Institute for Meteorology, Leipzig University, Leipzig, Germany

Johannes Quaas orcid.org/0000-0001-7057-194X
Institute for Meteorology, Leipzig University, Leipzig, Germany

Olivia Linke orcid.org/0000-0002-5286-2185
Department of Meteorology, Stockholm University, Stockholm, Sweden; Formerly at Institute for Meteorology, Leipzig University, Leipzig, Germany

Karsten Haustein orcid.org/0000-0003-3126-7851
Institute for Meteorology, Leipzig University, Leipzig, Germany

REFERENCES

Alekseev, G.V., Glok, N.I., Vyazilova, A.E. and **Kharlanenkova, N.E.** (2020) Climate change in the arctic: causes and mechanisms. *IOP Conference Series: Earth and Environmental Science*, 606(1): 012002. DOI: https://doi.org/10.1088/1755-1315/606/1/012002

Allen, R.J. and **Sherwood, S.C.** (2011) The impact of natural versus anthropogenic aerosols on atmospheric circulation in the community atmosphere model. *Climate Dynamics*, 36(9): 1959–1978. DOI: https://doi.org/10.1007/s00382-010-0898-8

Andrews, T. (2019) Mohc hadgem3-gc31-ll model output prepared for cmip6 rfmip piclim-control. DOI: https://doi.org/10.22033/ESGF/CMIP6.6275

Andrews, T. (2020) Mohc hadgem3-gc31-ll model output prepared for cmip6 rfmip piclim-histaer. DOI: https://doi.org/10.22033/ESGF/CMIP6.6281

Bellouin, N., Quaas, J., Gryspeerdt, E., Kinne, S., Stier, P., Watson-Parris, D., Boucher, O., Carslaw, K.S., Christensen, M., Daniau, A.-L., Dufresne, J.-L., Feingold, G., Fiedler, S., Forster, P., Gettelman, A., Haywood, J.M., Lohmann, U., Malavelle, F., Mauritsen, T., McCoy, D.T., Myhre, G., Mülmenstädt, J., Neubauer, D., Possner, A., Rugenstein, M., Sato, Y., Schulz, M., Schwartz, S.E., Sourdeval, O., Storelvmo, T., Toll, V., Winker, D. and **Stevens, B.** (2020) Bounding global aerosol radiative forcing of climate change. *Reviews of Geophysics*, 58(1): e2019RG000660. DOI: https://doi.org/10.1029/2019RG000660

Block, K., Schneider, F.A., Mülmenstädt, J., Salzmann, M. and **Quaas, J.** (2020) Climate models disagree on the sign of total radiative feedback in the arctic. *Tellus A: Dynamic Meteorology and Oceanography*, 72(1): 1696139. DOI: https://doi.org/10.1080/16000870.2019.1696139

Boucher, O., Denvil, S., Levavasseur, G., Cozic, A., Caubel, A., Foujols, M.-A., Meurdesoif, Y., Balkanski, Y., Checa-Garcia, R., Hauglustaine, D., Bekki, S. and **Marchand, M.** (2020a) Ipsl ipsl-cm6a-lr-inca model output prepared for cmip6 rfmip piclim-aer. DOI: https://doi.org/10.22033/ESGF/CMIP6.14604

Boucher, O., Denvil, S., Levavasseur, G., Cozic, A., Caubel, A., Foujols, M.-A., Meurdesoif, Y., Balkanski, Y., Checa-Garcia, R., Hauglustaine, D., Bekki, S. and **Marchand, M.** (2020b) Ipsl ipsl-cm6a-lr-inca model output prepared for cmip6 rfmip piclim-control. DOI: https://doi.org/10.22033/ESGF/CMIP6.14606

Boucher, O., Servonnat, J., Albright, A.L., Aumont, O., Balkanski, Y., Bastrikov, V., Bekki, S., Bonnet, R., Bony, S., Bopp, L., Braconnot, P., Brockmann, P., Cadule, P., Caubel, A., Cheruy, F., Codron, F., Cozic, A., Cugnet, D., D'Andrea, F., Davini, P., de Lavergne, C., Denvil, S., Deshayes, J., Devilliers, M., Ducharne, A., Dufresne, J., Dupont, E., Éthé, C., Fairhead, L., Falletti, L., Flavoni, S., Foujols, M., Gardoll, S., Gastineau, G., Ghattas, J., Grandpeix, J., Guenet, B., Guez, Lionel, E., Guilyardi, E., Guimberteau, M., Hauglustaine, D., Hourdin, F., Idelkadi, A., Joussaume, S., Kageyama, M., Khodri, M., Krinner, G., Lebas, N., Levavasseur, G., Lévy, C., Li, L., Lott, F., Lurton, T., Luyssaert, S., Madec, G., Madeleine, J., Maignan, F., Marchand, M., Marti, O., Mellul, L., Meurdesoif, Y., Mignot, J., Musat, I., Ottlé, C., Peylin, P., Planton, Y., Polcher, J., Rio, C., Rochetin, N., Rousset, C., Sepulchre, P., Sima, A., Swingedouw, D., Thiéblemont, R., Traore, A.K., Vancoppenolle, M., Vial, J., Vialard, J., Viovy, N. and **Vuichard, N.** (2020c) Presentation and evaluation of the ipsl-cm6a-lr climate model. *Journal of Advances in Modeling Earth Systems*, 12(7). DOI: https://doi.org/10.1029/2019MS002010

Calì Quaglia, F., Meloni, D., Muscari, G., Di Iorio, T., Ciardini, V., Pace, G., Becagli, S., Di Bernardino, A., Cacciani, M., Hannigan, J.W., Ortega, I. and **di Sarra, A.G.** (2022) On the radiative impact of biomass-burning aerosols in the arctic: The august 2017 case study. *Remote Sensing*, 14(2): 313. DOI: https://doi.org/10.3390/rs14020313

Chung, C.E. and **Ramanathan, V.** (2003) South asian haze forcing: Remote impacts with implications to enso and ao. *Journal of Climate*, 16(11): 1791–1806. DOI: https://doi.org/10.1175/1520-0442(2003)016<1791:SAHFRI>2.0.CO;2

Ciais, P., Sabine, C., Bala, G., Bopp, L., Brovkin, V., Canadell, J., Chhabra, A., DeFries, R., Galloway, J., Heimann, M., Jones, C., Le Quéré, C., Myneni, R., Piao, S. and **Thornton, P.** (2013) *Carbon and Other Biogeochemical Cycles*, book section 6, page 465–570. Cambridge, United Kingdom and New York, NY, USA: Cambridge University Press.

Cole, J.N., Li, J., Swart, N.C., Kharin, V.V., Lazare, M., Scinocca, J.F., Gillett, N.P., Anstey, J., Arora, V., Christian, J.R., Jiao, Y., Lee, W.G., Majaess, F., Saenko, O.A., Seiler, C., Seinen, C., Shao, A., Solheim, L., von Salzen, K., Yang, D., Winter, B. and **Sigmond, M.** (2019a) Cccma canesm5 model output prepared for cmip6 rfmip piclim-aer.

Cole, J.N., Li, J., Swart, N.C., Kharin, V.V., Lazare, M., Scinocca, J.F., Gillett, N.P., Anstey, J., Arora, V., Christian, J.R., Jiao, Y., Lee, W.G., Majaess, F., Saenko, O.A., Seiler, C., Seinen, C., Shao, A., Solheim, L., von Salzen, K., Yang, D., Winter, B. and **Sigmond, M.** (2019b) Cccma canesm5 model output prepared for cmip6 rfmip piclim-control.

Cole, J.N., Li, J., Swart, N.C., Kharin, V.V., Lazare, M., Scinocca, J.F., Gillett, N.P., Anstey, J., Arora, V., Christian, J.R., Jiao, Y., Lee, W.G., Majaess, F., Saenko, O.A., Seiler, C., Seinen, C., Shao, A., Solheim, L., von Salzen, K., Yang, D., Winter, B. and **Sigmond, M.** (2019c) Cccma canesm5 model output prepared for cmip6 rfmip piclim-histaer. DOI: https://doi.org/10.22033/ESGF/CMIP6.3664

Craigmile, P.F. and **Guttorp, P.** (2021) A combined estimate of global temperature. *Environmetrics*, 33(3). DOI: https://doi.org/10.1002/env.2706

Dai, A., Luo, D., Song, M. and **Liu, J.** (2019) Arctic amplification is caused by sea-ice loss under increasing CO_2. *Nature Communications*, 10(1). DOI: https://doi.org/10.1038/s41467-018-07954-9

DeMott, P.J., Prenni, A.J., Liu, X., Kreidenweis, S.M., Petters, M.D., Twohy, C.H., Richardson, M.S., Eidhammer, T. and **Rogers, D.C.** (2010) Predicting global atmospheric ice nuclei distributions and their impacts on climate. *Proceedings of the National Academy of Sciences*, 107(25): 11217–11222. DOI: https://doi.org/10.1073/pnas.0910818107

Döscher, R., Acosta, M., Alessandri, A., Anthoni, P., Arsouze, T., Bergman, T., Bernardello, R., Boussetta, S., Caron, L.-P., Carver, G., Castrillo, M., Catalano, F., Cvijanovic, I., Davini, P., Dekker, E., Doblas-Reyes, F.J., Docquier, D., Echevarria, P., Fladrich, U., Fuentes-Franco, R., Gröger, M., v. Hardenberg, J., Hieronymus, J., Karami, M.P., Keskinen, J.-P., Koenigk, T., Makkonen, R., Massonnet, F., Ménégoz, M., Miller, P.A., Moreno-Chamarro, E., Nieradzik, L., van Noije, T., Nolan, P., O'Donnell, D., Ollinaho, P., van den Oord, G., Ortega, P., Prims, O.T., Ramos, A., Reerink, T., Rousset, C., Ruprich-Robert, Y., Le Sager, P., Schmith, T., Schrödner, R., Serva, F., Sicardi, V., Sloth Madsen, M., Smith, B., Tian, T., Tourigny, E., Uotila, P., Vancoppenolle, M., Wang, S., Wårlind, D., Willén, U., Wyser, K., Yang, S., Yepes-Arbós, X. and **Zhang, Q.** (2022) The ec-earth3 earth system model for the coupled model intercomparison project 6. *Geoscientific Model Development*, 15(7): 2973–3020. DOI: https://doi.org/10.5194/gmd-15-2973-2022

EC-Earth Consortium (2020a) Ec-earth-consortium ec-earth3 model output prepared for cmip6 rfmip piclim-aer.

EC-Earth Consortium (2020b) Ec-earth-consortium ec-earth3 model output prepared for cmip6 rfmip piclim-control.

Eyring, V., Bony, S., Meehl, G.A., Senior, C.A., Stevens, B., Stouffer, R.J. and **Taylor, K.E.** (2016) Overview of the coupled model intercomparison project phase 6 (cmip6) experimental design and organization. *Geoscientific Model Development*, 9(5): 1937–1958. DOI: https://doi.org/10.5194/gmd-9-1937-2016

Feldl, N. and **Roe, G.H.** (2013) The nonlinear and nonlocal nature of climate feedbacks. *Journal of Climate*, 26(21): 8289–8304. DOI: https://doi.org/10.1175/JCLI-D-12-00631.1

Forster, P.M., Richardson, T., Maycock, A.C., Smith, C.J., Samset, B.H., Myhre, G., Andrews, T., Pincus, R. and **Schulz, M.** (2016) Recommendations for diagnosing effective radiative forcing from climate models for cmip6. *Journal of Geophysical Research: Atmospheres*, 121(20). DOI: https://doi.org/10.1002/2016JD025320

Guy, H., Brooks, I.M., Carslaw, K.S., Murray, B.J., Walden, V.P., Shupe, M.D., Pettersen, C., Turner, D.D., Cox, C.J., Neff, W.D., Bennartz, R., and **Neely, R.R. III.** (2021) Controls on surface aerosol particle number concentrations and aerosol-limited cloud regimes over the central greenland ice sheet. *Atmospheric Chemistry and Physics*, 21(19): 15351–15374. DOI: https://doi.org/10.5194/acp-21-15351-2021

Hansen, J., Ruedy, R., Sato, M. and **Lo, K.** (2010) Global surface temperature change. *Reviews of Geophysics*, 48(4). DOI: https://doi.org/10.1029/2010RG000345

Hoskins, B.J. and **James, I.N.** (2014) *Fluid Dynamics of the Midlatitude Atmosphere*. Wiley. DOI: https://doi.org/10.1002/9781118526002

Huang, H. and **Huang, Y**. (2023a) Data for ERA5 radiative kernels. DOI: https://doi.org/10.17632/vmg3s67568.4

Huang, H. and **Huang, Y.** (2023b) Radiative sensitivity quantified by a new set of radiation flux kernels based on the ecmwf reanalysis v5 (era5). *Earth System Science Data*, 15(7): 3001–3021. DOI: https://doi.org/10.5194/essd-15-3001-2023

Huang, Y., Xia, Y. and **Tan, X.** (2017) On the pattern of CO_2 radiative forcing and poleward energy transport. *Journal of Geophysical Research: Atmospheres*, 122(20): 10,578–10,593. DOI: https://doi.org/10.1002/2017JD027221

Kiehl, J.T. and **Trenberth, K.E.** (1997) Earth's annual global mean energy budget. *Bulletin of the American Meteorological Society*, 78(2): 197–208. DOI: https://doi.org/10.1175/1520-0477(1997)078<0197:EAGMEB>2.0.CO;2

Laîné, A., Yoshimori, M. and **Abe-Ouchi, A.** (2016) Surface arctic amplification factors in cmip5 models: Land and oceanic surfaces and seasonality. *Journal of Climate*, 29(9): 3297–3316. DOI: https://doi.org/10.1175/JCLI-D-15-0497.1

Law, K.S., Stohl, A., Quinn, P.K., Brock, C.A., Burkhart, J.F., Paris, J.-D., Ancellet, G., Singh, H.B., Roiger, A., Schlager, H., Dibb, J., Jacob, D.J., Arnold, S.R., Pelon, J. and **Thomas, J.L.** (2014) Arctic air pollution: New insights from polarcat-ipy. *Bulletin of the American Meteorological Society*, 95(12): 1873–1895. DOI: https://doi.org/10.1175/BAMS-D-13-00017.1

Limpasuvan, V. and **Hartmann, D.L.** (2000) Wave-maintained annular modes of climate variability. *Journal of Climate*, 13(24): 4414–4429. DOI: https://doi.org/10.1175/1520-0442(2000)013<4414:WMAMOC>2.0.CO;2

Linke, O., Quaas, J., Baumer, F., Becker, S., Chylik, J., Dahlke, S., Ehrlich, A., Handorf, D., Jacobi, C., Kalesse-Los, H., Lelli, L., Mehrdad, S., Neggers, R.A.J., Riebold, J., Saavedra Garfias, P., Schnierstein, N., Shupe, M.D., Smith, C., Spreen, G., Verneuil, B., Vinjamuri, K.S., Vountas, M. and **Wendisch, M.** (2023) Constraints on simulated past arctic amplification and lapse rate feedback from observations. *Atmospheric Chemistry and Physics*, 23(17): 9963–9992. DOI: https://doi.org/10.5194/acp-23-9963-2023

Maturilli, M. and **Kayser, M.** (2017) Arctic warming, moisture increase and circulation changes observed in the ny-ålesund homogenized radiosonde record. *Theoretical and Applied Climatology*, 130(1): 1–17. DOI: https://doi.org/10.1007/s00704-016-1864-0

Mauritsen, T., Bader, J., Becker, T., Behrens, J., Bittner, M., Brokopf, R., Brovkin, V., Claussen, M., Crueger, T., Esch, M., Fast, I., Fiedler, S., Fläschner, D., Gayler, V., Giorgetta, M., Goll, D.S., Haak, H., Hagemann, S., Hedemann, C., Hohenegger, C., Ilyina, T., Jahns, T., Jimenéz-de-la-Cuesta, D., Jungclaus, J., Kleinen, T., Kloster, S., Kracher, D., Kinne, S., Kleberg, D., Lasslop, G., Kornblueh, L., Marotzke, J., Matei, D., Meraner, K., Mikolajewicz, U., Modali, K., Möbis, B., Müller, W.A., Nabel, J.E.M.S., Nam, C.C.W., Notz, D., Nyawira, S., Paulsen, H., Peters, K., Pincus, R., Pohlmann, H., Pongratz, J., Popp, M., Raddatz, T.J., Rast, S., Redler, R., Reick, C.H., Rohrschneider, T., Schemann, V., Schmidt, H., Schnur, R., Schulzweida, U., Six, K.D., Stein, L., Stemmler, I., Stevens, B., von Storch, J., Tian, F., Voigt, A., Vrese, P., Wieners, K., Wilkenskjeld, S., Winkler, A. and **Roeckner, E.** (2019) Developments in the mpi-m earth system model version 1.2 (mpi-esm1.2) and its response to increasing CO_2. *Journal of Advances in Modeling Earth Systems*, 11(4): 998–1038. DOI: https://doi.org/10.1029/2018MS001400

Mauritsen, T., Graversen, R., Klocke, D., Langen, P., Stevens, B. and **Tomassini, L.** (2013) Climate feedback efficiency and synergy. *Climate Dynamics*, 41(9–10): 2539–2554. DOI: https://doi.org/10.1007/s00382-013-1808-7

Morice, C.P., Kennedy, J.J., Rayner, N.A., Winn, J.P., Hogan, E., Killick, R.E., Dunn, R.J.H., Osborn, T.J., Jones, P.D. and **Simpson, I.R.** (2021) An updated assessment of near-surface temperature change from 1850: The hadcrut5 data set. *Journal of Geophysical Research: Atmospheres*, 126(3): e2019JD032361. DOI: https://doi.org/10.1029/2019JD032361

Myhre, G., Shindell, D., Bréon, F.-M., Collins, W., Fuglestvedt, J., Huang, J., Koch, D., Lamarque, J.-F., Lee, D., Mendoza, B., Nakajima, T., Robock, A., Stephens, G., Takemura, T. and **Zhang, H.** (2013) Anthropogenic and natural radiative forcing. In: Stocker, T., Qin, D., Plattner, G.-K., Tignor, M., Allen, S., Boschung, J., Nauels, A., Xia, Y., Bex, V. and Midgley, P. (eds.) *Climate Change 2013: The Physical Science Basis. Contribution of Working Group I to the Fifth Assessment Report of the Intergovernmental Panel on Climate Change*, book section 8. Cambridge, United Kingdom and New York, NY, USA: Cambridge University Press, pp. 659–740. DOI: https://doi.org/10.1017/CBO9781107415324.018

Naik, V., Szopa, S., Adhikary, B., Artaxo, P., Berntsen, T., Collins, W.D., Fuzzi, S., Gallardo, L., Kiendler Scharr, A., Klimont, Z., Liao, H., Unger, N. and **Zanis, P.** (2021) Short-lived climate forcers. In Masson-Delmotte, V., Zhai, P., Pirani, A., Connors, S.L., Péan, C., Berger, S., Caud, N., Chen, Y., Goldfarb, L., Gomis, M.I., Huang, M., Leitzell, K., Lonnoy, E., Matthews, J.B.R., Maycock, T.K., Waterfield, T., Yelekçi, O., Yu, R. and Zhou, B. (eds.) *Climate Change 2021: The Physical Science Basis. Contribution of Working Group I to the Sixth Assessment Report of the Intergovernmental Panel on Climate Change*, book section 6. Cambridge, United Kingdom and New York, NY, USA: Cambridge University Press.

Neubauer, D., Ferrachat, S., Siegenthaler-Le Drian, C., Stoll, J., Folini, D.S., Tegen, I., Wieners, K.-H., Mauritsen, T., Stemmler, I., Barthel, S., Bey, I., Daskalakis, N., Heinold, B., Kokkola, H., Partridge, D., Rast, S., Schmidt, H., Schutgens, N., Stanelle, T., Stier, P., Watson-Parris, D. and **Lohmann, U.** (2019a) Hammoz-consortium mpi-esm1.2-ham model output prepared for cmip6 rfmip piclim-aer.

Neubauer, D., Ferrachat, S., Siegenthaler-Le Drian, C., Stoll, J., Folini, D.S., Tegen, I., Wieners, K.-H., Mauritsen, T., Stemmler, I., Barthel, S., Bey, I., Daskalakis, N., Heinold, B., Kokkola, H., Partridge, D., Rast, S., Schmidt, H., Schutgens, N., Stanelle, T., Stier, P., Watson-Parris, D. and **Lohmann, U.** (2019b) Hammoz-consortium mpi-esm1.2-ham model output prepared for cmip6 rfmip piclim-control.

Noyelle, R., Faranda, D. and **Yiou, P.** (2022) Modeling the northern eddy-driven jet stream position and wind speed variability with stochastic coupled non-linear lattices. DOI: https://doi.org/10.5194/egusphere-egu22-1250

O'Connor, F. (2019a) Mohc ukesm1.0-ll model output prepared for cmip6 aerchemmip piclim-aer. DOI: https://doi.org/10.22033/ESGF/CMIP6.6270

O'Connor, F. (2019b) Mohc ukesm1.0-ll model output prepared for cmip6 aerchemmip piclim-control. DOI: https://doi.org/10.22033/ESGF/CMIP6.6276

Oliviè, D.J.L., Bentsen, M., Seland, O., Toniazzo, T., Gjermundsen, A., Graff, L.S., Debernard, J.B., Gupta, A.K., He, Y., Kirkevåg, A., Schwinger, J., Tjiputra, J., Aas, K.S., Bethke, I., Fan, Y., Griesfeller, J., Grini, A., Guo, C., Ilicak, M., Karset, I.H.H., Landgren, O.A., Liakka, J., Moseid, K.O., Nummelin, A., Spensberger, C., Tang, H., Zhang, Z., Heinze, C., Iversen, T. and **Schulz, M.** (2019a) Ncc noresm2-lm model output prepared for cmip6 rfmip piclim-control. DOI: https://doi.org/10.22033/ESGF/CMIP6.8179

Oliviè, D.J.L., Bentsen, M., Seland, O., Toniazzo, T., Gjermundsen, A., Graff, L.S., Debernard, J.B., Gupta, A.K., He, Y., Kirkevåg, A., Schwinger, J., Tjiputra, J., Aas, K.S., Bethke, I., Fan, Y., Griesfeller, J., Grini, A., Guo, C., Ilicak, M., Karset, I.H.H., Landgren, O.A., Liakka, J., Moseid, K.O., Nummelin, A., Spensberger, C., Tang, H., Zhang, Z., Heinze, C., Iversen, T. and **Schulz, M.** (2019b) Ncc noresm2-lm model output prepared for cmip6 rfmip piclim-histaer. DOI: https://doi.org/10.22033/ESGF/CMIP6.8189

O'Neill, B.C., Tebaldi, C., van Vuuren, D.P., Eyring, V., Friedlingstein, P., Hurtt, G., Knutti, R., Kriegler, E., Lamarque, J.-F., Lowe, J., Meehl, G.A., Moss, R., Riahi, K. and **Sanderson, B.M.** (2016) The scenario model intercomparison project (scenariomip) for cmip6. *Geoscientific Model Development*, 9(9): 3461–3482. DOI: https://doi.org/10.5194/gmd-9-3461-2016

Pendergrass, A.G., Conley, A. and **Vitt, F.M.** (2018) Surface and top-of-atmosphere radiative feedback kernels for cesm-cam5. *Earth System Science Data*, 10(1): 317–324. DOI: https://doi.org/10.5194/essd-10-317-2018

Pincus, R., Forster, P.M. and **Stevens, B.** (2016) The radiative forcing model intercomparison project (rfmip): experimental protocol for cmip6. *Geoscientific Model Development*, 9(9): 3447–3460. DOI: https://doi.org/10.5194/gmd-9-3447-2016

Previdi, M., Smith, K.L. and **Polvani, L.M.** (2021) Arctic amplification of climate change: a review of underlying mechanisms. *Environmental Research Letters*, 16(9): 093003. DOI: https://doi.org/10.1088/1748-9326/ac1c29

Pritchard, H.D., Arthern, R.J., Vaughan, D.G. and **Edwards, L.A.** (2009) Extensive dynamic thinning on the margins of the greenland and antarctic ice sheets. *Nature*, 461(7266): 971–975. DOI: https://doi.org/10.1038/nature08471

Qu, W., Huang, F., Zhao, J., Du, L. and **Cao, Y.** (2021) Volcanic activity sparks the arctic oscillation. *Scientific Reports*, 11(1): 15839. DOI: https://doi.org/10.1038/s41598-021-94935-6

Rantanen, M., Karpechko, A.Y., Lipponen, A., Nordling, K., Hyvärinen, O., Ruosteenoja, K., Vihma, T. and **Laaksonen, A.** (2022) The Arctic has warmed nearly four times faster than the globe since 1979. *Communications Earth and Environment*, 3(1): 168. DOI: https://doi.org/10.1038/s43247-022-00498-3

Salvi, P., Ceppi, P. and **Gregory, J.M.** (2022) Interpreting differences in radiative feedbacks from aerosols versus greenhouse gases. *Geophysical Research Letters*, 49(8). DOI: https://doi.org/10.1029/2022GL097766

Schuenemann, K.C., Cassano, J.J. and **Finnis, J.** (2009) Synoptic forcing of precipitation over greenland: Climatology for 1961–99. *Journal of Hydrometeorology*, 10(1): 60–78. DOI: https://doi.org/10.1175/2008JHM1014.1

Seferian, R. (2019a) Cnrm-cerfacs cnrm-esm2-1 model output prepared for cmip6 rfmip piclim-aer.

Seferian, R. (2019b) Cnrm-cerfacs cnrm-esm2-1 model output prepared for cmip6 rfmip piclim-control.

Séférian, R., Nabat, P., Michou, M., Saint-Martin, D., Voldoire, A., Colin, J., Decharme, B., Delire, C., Berthet, S., Chevallier, M., Sénési, S., Franchisteguy, L., Vial, J., Mallet, M., Joetzjer, E., Geoffroy, O., Guérémy, J., Moine, M., Msadek, R., Ribes, A., Rocher, M., Roehrig, R., Salas-y-Mélia, D., Sanchez, E., Terray, L., Valcke, S., Waldman, R., Aumont, O., Bopp, L., Deshayes, J., Éthé, C. and **Madec, G.** (2019) Evaluation of cnrm earth system model, cnrm-esm2-1: Role of earth system processes in present-day and future climate. *Journal of Advances in Modeling Earth Systems*, 11(12): 4182–4227. DOI: https://doi.org/10.1029/2019MS001791

Sekiguchi, M. and **Shiogama, H.** (2019a) Miroc miroc6 model output prepared for cmip6 rfmip piclim-aer.

Sekiguchi, M. and **Shiogama, H.** (2019b) Miroc miroc6 model output prepared for cmip6 rfmip piclim-control.

Sekiguchi, M. and **Shiogama, H.** (2019c) Miroc miroc6 model output prepared for cmip6 rfmip piclim-histaer. DOI: https://doi.org/10.22033/ESGF/CMIP6.5700

Seland, O., Bentsen, M., Olivié, D., Toniazzo, T., Gjermundsen, A., Graff, L.S., Debernard, J.B., Gupta, A.K., He, Y.-C., Kirkevåg, A., Schwinger, J., Tjiputra, J., Aas, K.S., Bethke, I., Fan, Y., Griesfeller, J., Grini, A., Guo, C., Ilicak, M., Karset, I.H.H., Landgren, O., Liakka, J., Moseid, K.O., Nummelin, A., Spensberger, C., Tang, H., Zhang, Z., Heinze, C., Iversen, T. and **Schulz, M.** (2020) Overview of the norwegian earth system model (noresm2) and key climate response of cmip6 deck, historical, and scenario simulations. *Geoscientific Model Development*, 13(12): 6165–6200. DOI: https://doi.org/10.5194/gmd-13-6165-2020

Sellar, A.A., Jones, C.G., Mulcahy, J.P., Tang, Y., Yool, A., Wiltshire, A., O'Connor, F.M., Stringer, M., Hill, R., Palmieri, J., Woodward, S., de Mora, L., Kuhlbrodt, T., Rumbold, S.T., Kelley, D.I., Ellis, R., Johnson, C.E., Walton, J., Abraham, N.L., Andrews, M.B., Andrews, T., Archibald, A.T., Berthou, S., Burke, E., Blockley, E., Carslaw, K., Dalvi, M., Edwards, J., Folberth, G.A., Gedney, N., Griffiths, P.T., Harper, A.B., Hendry, M.A., Hewitt, A.J., Johnson, B., Jones, A., Jones, C.D., Keeble, J., Liddicoat, S., Morgenstern, O., Parker, R.J., Predoi, V., Robertson, E., Siahaan, A., Smith, R.S., Swaminathan, R., Woodhouse, M.T., Zeng, G. and **Zerroukat, M.** (2019) Ukesm1: Description and evaluation of the u.k. earth system model. *Journal of Advances in Modeling Earth Systems*, 11(12): 4513–4558. DOI: https://doi.org/10.1029/2019MS001739

Shell, K.M., Kiehl, J.T. and **Shields, C.A.** (2008) Using the radiative kernel technique to calculate climate feedbacks in ncar's community atmospheric model. *Journal of Climate*, 21(10): 2269–2282. DOI: https://doi.org/10.1175/2007JCLI2044.1

Smith, C.J., Kramer, R.J., Myhre, G., Alterskjær, K., Collins, W., Sima, A., Boucher, O., Dufresne, J.-L., Nabat, P., Michou, M., Yukimoto, S., Cole, J., Paynter, D., Shiogama, H., O'Connor, F.M., Robertson, E., Wiltshire, A., Andrews, T., Hannay, C., Miller, R., Nazarenko, L., Kirkevåg, A., Olivié, D., Fiedler, S., Lewinschal, A., Mackallah, C., Dix, M., Pincus, R. and **Forster, P.M.** (2020a) Effective radiative forcing and adjustments in cmip6 models. *Atmospheric Chemistry and Physics*, 20(16): 9591–9618. DOI: https://doi.org/10.5194/acp-20-9591-2020

Smith, C.J., Kramer, R.J. and **Sima, A.** (2020b) The hadgem3-ga7.1 radiative kernel: the importance of a well-resolved stratosphere. *Earth System Science Data*, 12(3): 2157–2168. DOI: https://doi.org/10.5194/essd-12-2157-2020

Soden, B.J. and **Held, I.M.** (2006) An assessment of climate feedbacks in coupled ocean–atmosphere models. *Journal of Climate*, 19(14): 3354–3360. DOI: https://doi.org/10.1175/JCLI3799.1

Soden, B.J., Held, I.M., Colman, R., Shell, K.M., Kiehl, J.T. and **Shields, C.A.** (2008) Quantifying climate feedbacks using radiative kernels. *Journal of Climate*, 21(14): 3504–3520. DOI: https://doi.org/10.1175/2007JCLI2110.1

Stone, R.S., Anderson, G.P., Shettle, E.P., Andrews, E., Loukachine, K., Dutton, E.G., Schaaf, C. and **Roman, M.O.** (2008) Radiative impact of boreal smoke in the arctic: Observed and modeled. *Journal of Geophysical Research: Atmospheres*, 113(D14). DOI: https://doi.org/10.1029/2007JD009657

Swart, N.C., Cole, J.N.S., Kharin, V.V., Lazare, M., Scinocca, J.F., Gillett, N.P., Anstey, J., Arora, V., Christian, J.R., Hanna, S., Jiao, Y., Lee, W.G., Majaess, F., Saenko, O.A., Seiler, C., Seinen, C., Shao, A., Sigmond, M., Solheim, L., von Salzen, K., Yang, D. and **Winter, B.** (2019) The canadian earth system model version 5 (canesm5.0.3). *Geoscientific Model Development*, 12(11): 4823–4873. DOI: https://doi.org/10.5194/gmd-12-4823-2019

Tatebe, H., Ogura, T., Nitta, T., Komuro, Y., Ogochi, K., Takemura, T., Sudo, K., Sekiguchi, M., Abe, M., Saito, F., Chikira, M., Watanabe, S., Mori, M., Hirota, N., Kawatani, Y., Mochizuki, T., Yoshimura, K., Takata, K., O'ishi, R., Yamazaki, D., Suzuki, T., Kurogi, M., Kataoka, T., Watanabe, M. and **Kimoto, M.** (2019) Description and basic evaluation of simulated mean state, internal variability, and climate sensitivity in miroc6. *Geoscientific Model Development*, 12(7): 2727–2765. DOI: https://doi.org/10.5194/gmd-12-2727-2019

Taylor, P.C., Boeke, R.C., Boisvert, L.N., Feldl, N., Henry, M., Huang, Y., Langen, P.L., Liu, W., Pithan, F., Sejas, S.A. and **Tan, I.** (2022) Process drivers, inter-model spread, and the path forward: A review of amplified arctic warming. *Frontiers in Earth Science*, 9. DOI: https://doi.org/10.3389/feart.2021.758361

Thompson, D.W.J. and **Wallace, J.M.** (2000) Annular modes in the extratropical circulation. Part I: Month-to-month variability. *Journal of Climate*, 13(5): 1000–1016. DOI: https://doi.org/10.1175/1520-0442(2000)013<1000:AMITEC>2.0.CO;2

Treffeisen, R., Tunved, P., Ström, J., Herber, A., Bareiss, J., Helbig, A., Stone, R.S., Hoyningen-Huene, W., Krejci, R., Stohl, A. and **Neuber, R.** (2007) Arctic smoke – aerosol characteristics during a record smoke event in the european arctic and its radiative impact. *Atmospheric Chemistry and Physics*, 7(11): 3035–3053. DOI: https://doi.org/10.5194/acp-7-3035-2007

Twomey, S. (1974) Pollution and the planetary albedo. *Atmospheric Environment (1967)*, 8(12): 1251–1256. DOI: https://doi.org/10.1016/0004-6981(74)90004-3

Voldoire, A. (2019a) Cnrm-cerfacs cnrm-cm6-1 model output prepared for cmip6 rfmip piclim-aer.

Voldoire, A. (2019b) Cnrm-cerfacs cnrm-cm6-1 model output prepared for cmip6 rfmip piclim-control.

Voldoire, A., Saint-Martin, D., Sénési, S., Decharme, B., Alias, A., Chevallier, M., Colin, J., Guérémy, J., Michou, M., Moine, M., Nabat, P., Roehrig, R., Salas y Mélia, D., Séférian, R., Valcke, S., Beau, I., Belamari, S., Berthet, S., Cassou, C., Cattiaux, J., Deshayes, J., Douville, H., Ethé, C., Franchistéguy, L., Geoffroy, O., Lévy, C., Madec, G., Meurdesoif, Y., Msadek, R., Ribes, A., Sanchez-Gomez, E., Terray, L. and **Waldman, R.** (2019) Evaluation of cmip6 deck experiments with cnrm-cm6-1. *Journal of Advances in Modeling Earth Systems*, 11(7): 2177–2213. DOI: https://doi.org/10.1029/2019MS001683

Wendisch, M., Brückner, M., Crewell, S., Ehrlich, A., Notholt, J., Lüpkes, C., Macke, A., Burrows, J.P., Rinke, A., Quaas, J., Maturilli, M., Schemann, V., Shupe, M.D., Akansu, E.F., Barrientos-Velasco, C., Bärfuss, K., Blechschmidt, A.-M., Block, K., Bougoudis, I., Bozem, H., Böckmann, C., Bracher, A., Bresson, H., Bretschneider, L., Buschmann, M., Chechin, D.G., Chylik, J., Dahlke, S., Deneke, H., Dethloff, K., Donth, T., Dorn, W., Dupuy, R., Ebell, K., Egerer, U., Engelmann, R., Eppers, O., Gerdes, R., Gierens, R., Gorodetskaya, I.V., Gottschalk, M., Griesche, H., Gryanik, V.M., Handorf, D., Harm-Altstädter, B., Hartmann, J., Hartmann, M., Heinold, B., Herber, A., Herrmann, H., Heygster, G., Höschel, I., Hofmann, Z., Hölemann, J., Hünerbein, A., Jafariserajehlou, S., Jäkel, E., Jacobi, C., Janout, M., Jansen, F., Jourdan, O., Jurányi, Z., Kalesse-Los, H., Kanzow, T., Käthner, R., Kliesch, L.L., Klingebiel, M., Knudsen, E.M., Kovács, T., Körtke, W., Krampe, D., Kretzschmar, J., Kreyling, D., Kulla, B., Kunkel, D., Lampert, A., Lauer, M., Lelli, L., von Lerber, A., Linke, O., Löhnert, U., Lonardi, M., Losa, S.N., Losch, M., Maahn, M., Mech, M., Mei, L., Mertes, S., Metzner, E., Mewes, D., Michaelis, J., Mioche, G., Moser, M., Nakoudi, K., Neggers, R., Neuber, R., Nomokonova, T., Oelker, J., Papakonstantinou-Presvelou, I., Pätzold, F., Pefanis, V.,

Pohl, C., van Pinxteren, M., Radovan, A., Rhein, M., Rex, M., Richter, A., Risse, N., Ritter, C., Rostosky, P., Rozanov, V.V., Donoso, E.R., Saavedra Garfias, P., Salzmann, M., Schacht, J., Schäfer, M., Schneider, J., Schnierstein, N., Seifert, P., Seo, S., Siebert, H., Soppa, M.A., Spreen, G., Stachlewska, I.S., Stapf, J., Stratmann, F., Tegen, I., Viceto, C., Voigt, C., Vountas, M., Walbröl, A., Walter, M., Wehner, B., Wex, H., Willmes, S., Zanatta, M. and **Zeppenfeld, S.** (2023) Atmospheric and surface processes, and feedback mechanisms determining arctic amplification: A review of first results and prospects of the (ac)3 project. *Bulletin of the American Meteorological Society*, 104(1): E208–E242. DOI: https://doi.org/10.1175/BAMS-D-21-0218.1

Williams, K.D., Copsey, D., Blockley, E.W., Bodas-Salcedo, A., Calvert, D., Comer, R., Davis, P., Graham, T., Hewitt, H.T., Hill, R., Hyder, P., Ineson, S., Johns, T.C., Keen, A.B., Lee, R.W., Megann, A., Milton, S.F., Rae, J.G.L., Roberts, M.J., Scaife, A.A., Schiemann, R., Storkey, D., Thorpe, L., Watterson, I.G., Walters, D.N., West, A., Wood, R.A., Woollings, T. and **Xavier, P.K.** (2018) The met office global coupled model 3.0 and 3.1 (gc3.0 and gc3.1) configurations. *Journal of Advances in Modeling Earth Systems*, 10(2): 357–380. DOI: https://doi.org/10.1002/2017MS001115

Yukimoto, S., Kawai, H., Koshiro, T., Oshima, N., Yoshida, K., Urakawa, S., Tsujino, H., Deushi, M., Tanaka, T., Hosaka, M., Yabu, S., Yoshimura, H., Shindo, E., Mizuta, R., Obata, A., Adachi, Y. and **Ishii, M.** (2019) The meteorological research institute earth system model version 2.0, mri-esm2.0: Description and basic evaluation of the physical component. *Journal of the Meteorological Society of Japan. Ser. II*, 97(5): 931–965. DOI: https://doi.org/10.2151/jmsj.2019-051

Yukimoto, S., Koshiro, T., Kawai, H., Oshima, N., Yoshida, K., Urakawa, S., Tsujino, H., Deushi, M., Tanaka, T., Hosaka, M., Yoshimura, H., Shindo, E., Mizuta, R., Ishii, M., Obata, A. and **Adachi, Y.** (2019a) Mri mri-esm2.0 model output prepared for cmip6 rfmip piclim-aer.

Yukimoto, S., Koshiro, T., Kawai, H., Oshima, N., Yoshida, K., Urakawa, S., Tsujino, H., Deushi, M., Tanaka, T., Hosaka, M., Yoshimura, H., Shindo, E., Mizuta, R., Ishii, M., Obata, A. and **Adachi, Y.** (2019b) Mri mri-esm2.0 model output prepared for cmip6 rfmip piclim-control.

Zanis, P., Akritidis, D., Georgoulias, A.K., Allen, R.J., Bauer, S.E., Boucher, O., Cole, J., Johnson, B., Deushi, M., Michou, M., Mulcahy, J., Nabat, P., Olivié, D., Oshima, N., Sima, A., Schulz, M., Takemura, T. and **Tsigaridis, K.** (2020) Fast responses on pre-industrial climate from present-day aerosols in a cmip6 multi-model study. *Atmospheric Chemistry and Physics*, 20(14): 8381–8404. DOI: https://doi.org/10.5194/acp-20-8381-2020

Zhou, Y. and **Savijärvi, H.** (2014) The effect of aerosols on long wave radiation and global warming. *Atmospheric Research*, 135–136:102–111. DOI: https://doi.org/10.1016/j.atmosres.2013.08.009

TO CITE THIS ARTICLE:
Al Hajjar, K., Dipu, S., Quaas, J., Linke, O. and Haustein, K. (2025) Exploring the Sensitivity of Arctic Winter Climate to Aerosol Loading as Simulated in CMIP6. *Tellus B: Chemical and Physical Meteorology* 77(1): 20–40. DOI: https://doi.org/10.16993/tellusb.1885

Submitted: 30 June 2025 **Accepted:** 11 November 2025 **Published:** 24 November 2025

COPYRIGHT:
© 2025 The Author(s). This is an open-access article distributed under the terms of the Creative Commons Attribution 4.0 International License (CC-BY 4.0), which permits unrestricted use, distribution, and reproduction in any medium, provided the original author and source are credited. See http://creativecommons.org/licenses/by/4.0/.

Tellus B: Chemical and Physical Meteorology is a peer-reviewed open access journal published by Stockholm University Press.